Interpret the figures and text by expanding on what is being illustrated, explaining procedures or techniques, indicating why it might be important or making connections to our class readings and laboratory work. Tell more than rewriting the caption. Try to use your interpretation to demonstrate additional knowledge beyond what is shown here. You should write on each page for about 10 minutes.

ACS Nano (2020) DOI: 10.1021/acsnano.9b07430

METHODS

To fabricate the well-ordered nanopore pattern in anodic aluminum oxide (AAO), we employed a two-step anodization method. A 1050 aluminum alloy (Al 99.5% min.) sheet with 0.5 mm thickness cut into 70 mm × 30 mm was used. The first anodization was conducted under 40 V in 0.3 M oxalic acid at 0 ° C for 6 h. The thick anodic oxide layer was removed in an aqueous solution with 1.8 wt % of CrO_3 + 6 wt % of H_3PO_4 at 65 ° C for 3 h. For the second anodization, the same condition as the first anodization was applied for 30 min. The surface nanopore structure was further modified by immersing it in 0.1 M phosphoric acid at 30 ° C for 60 h. On the AAO templates, we deposited Y_2O_3 by ALD as previously reported.[17] An yttrium precursor, $Y(iPrCp)_2(N\text{-}iPr\text{-}amd)$, provided by the Air Liquide Korea company, was evaporated at 130 ° C in a stainless-steel bubbler to obtain sufficient vapor pressure. The vaporized precursor molecules and H_2O were transported into the reaction chamber by Ar carrier gas.

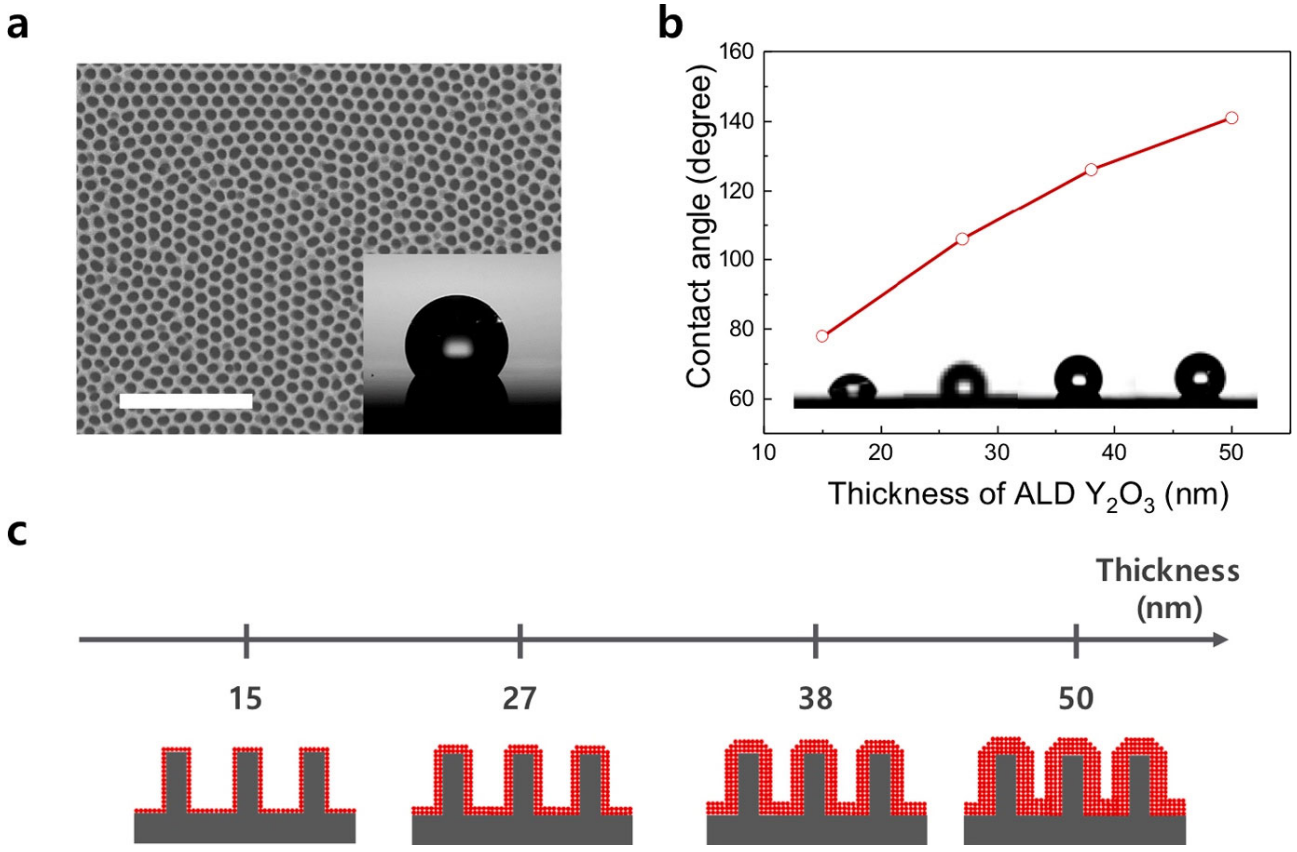

Figure 5. Y_2O_3-coated AAO substrate. (a) SEM image of AAO substrate. The inset shows wettability of 50 nm ALD Y_2O_3 on AAO. (b) WCAs change of Y_2O_3/AAO substrate with varying Y_2O_3 thickness. (c) Schematic of ALD Y_2O_3 films deposited with different thicknesses of 15, 27, 38, and 50 nm on AAO.

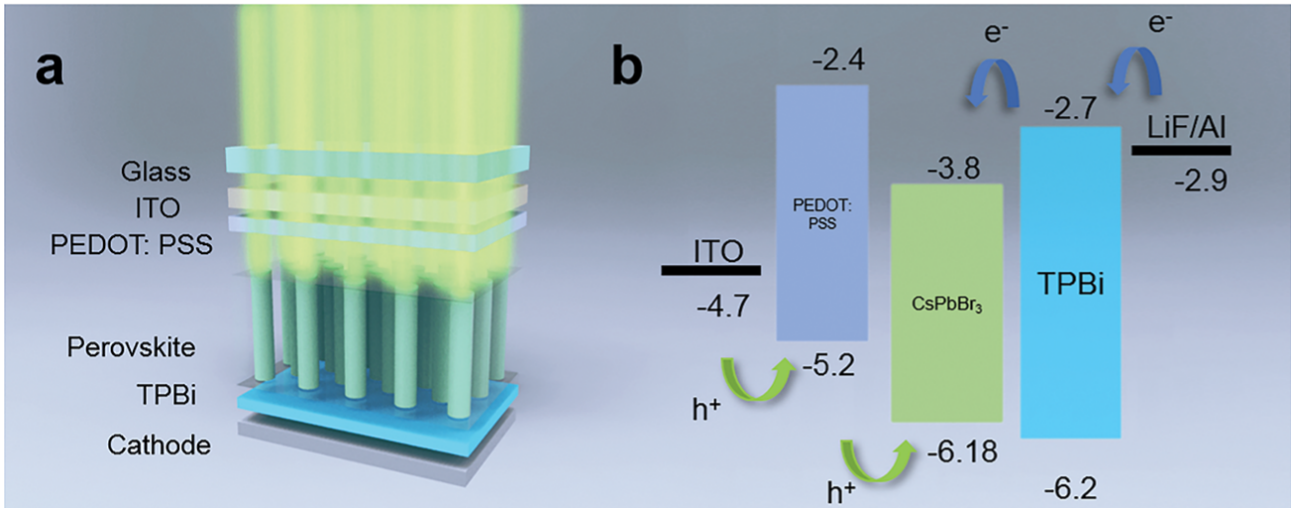

Figure 1. Perovskite nanophotonic wire (PNW) LED device structure and fabrication process. (a) Diagram of the PNW LED device using poly(3,4-ethylene dioxythiophene)-poly(styrenesulfonate) (PEDOT:PSS), $CsPbBr_3$ PNW, and 2,2',2"-(1,3,5-benzinetriyl)tris(1-phenyl-1*H*-benzimidazole) (TPBi) (b) Band energy diagram of the PNW LED device.

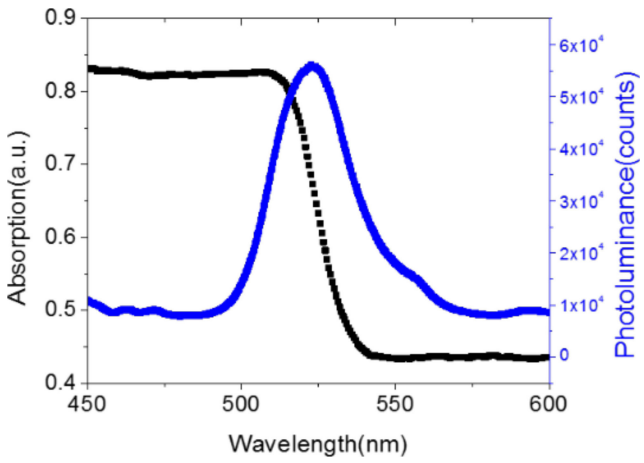

Figure S2. Absorption and photoluminescence spectra of the PNWs

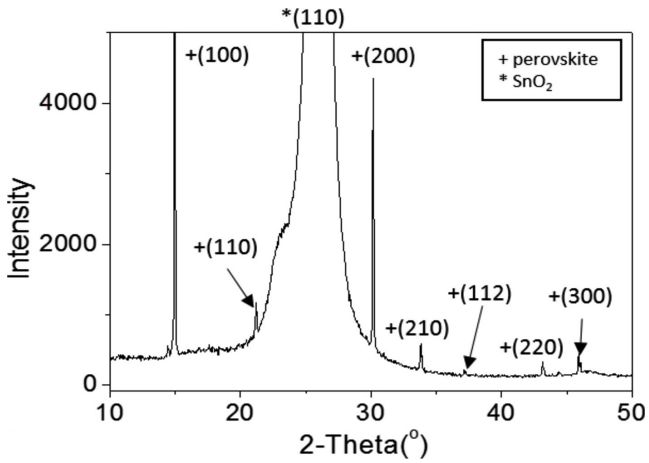

Figure S3. XRD of PNWs on ITO glass

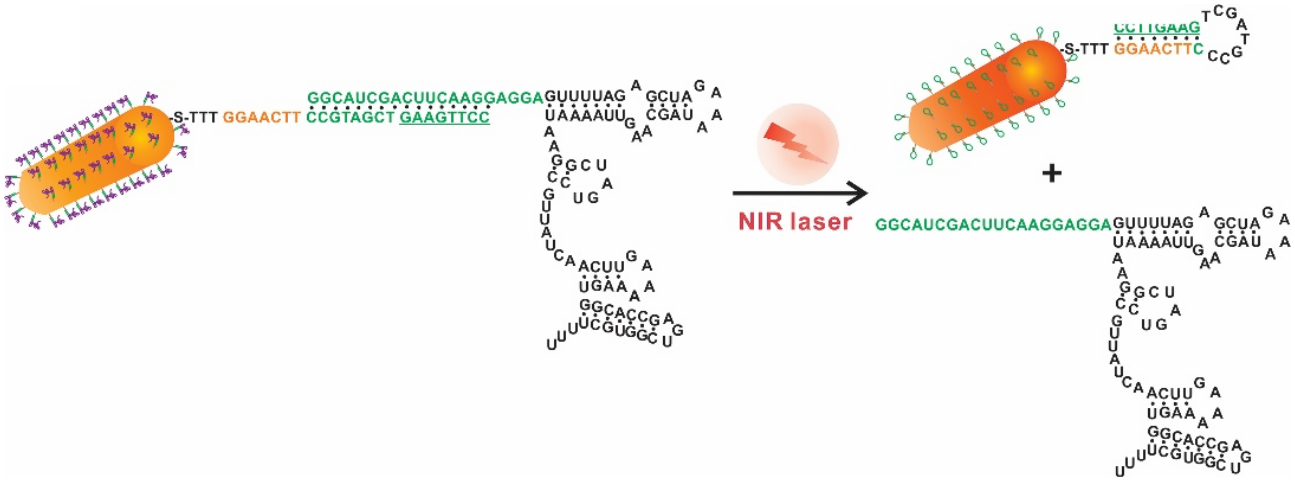

Figure S1. Irradiation of the laser activated CRISPR/Cas9 nano-machine (LACM) with a near-infrared laser produced heat, which dissociated the sgRNA from the protector strand. When separated from the sgRNA, the protector sequence formed spontaneously a hairpin structure, preventing it from re-hybridization with the sgRNA. The released sgRNA proceeded with CRISPR/Cas9 genome editing.

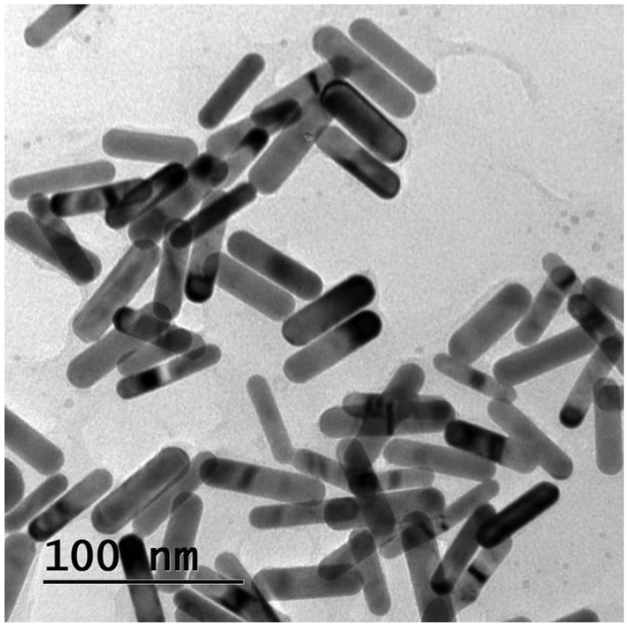

Figure S7. Transmission electron microscopy (TEM) image of LACM. The scale bar is 100 nm. TEM image shows that AuNR remained uniform in shape and size after conjugation of the protector-sgRNA hybrids.

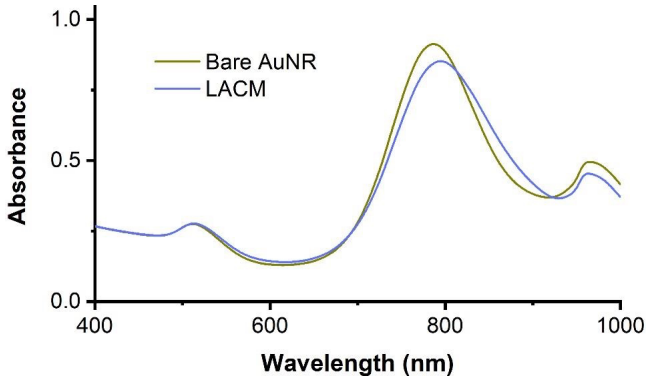

Figure S9. Ultraviolet/Visible absorbance spectra of bare AuNR and LACM. Similar absorbance spectra with maximum absorbance at ~800 nm suggests that there is no aggregation of either the bare AuNR or the LACM construct.

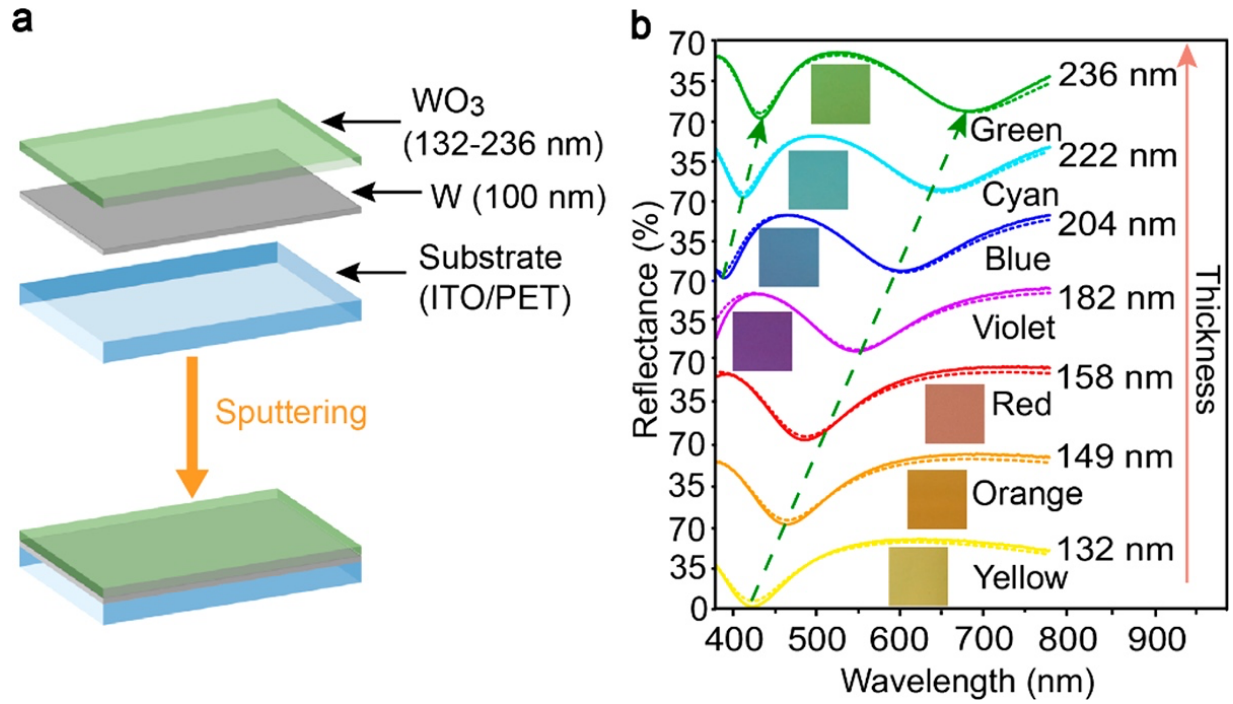

Figure 1. (a) Schematic diagram of the layered structure of the F−P cavity-type electrochromic supercapacitor electrodes. (b) Simulated (dashed line) and measured (solid line) reflection spectra. Inset: optical images of the F−P cavity-type electrochromic supercapacitor electrodes with different thicknesses of the WO_3 layer.

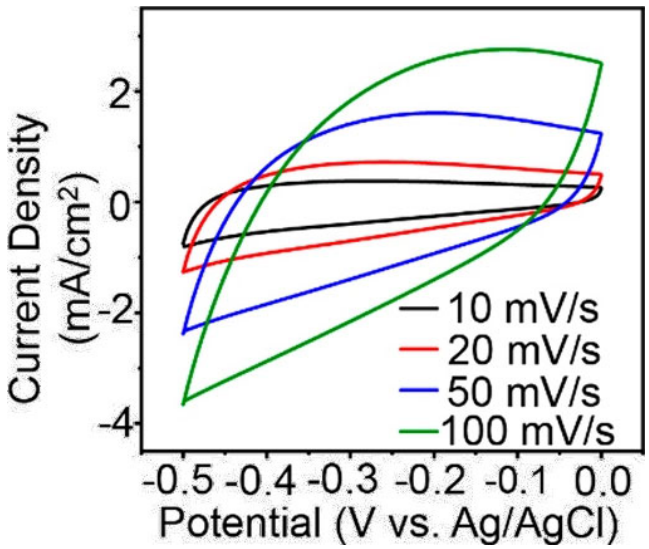

Figure 2. CV curves of an F−P cavity-type electrochromic supercapacitor electrode with a 132 nm thick WO_3 layer recorded in 1 M H_2SO_4 at different potential scan rates Pt and Ag/AgCl were used as the counter electrode and the reference electrode, respectively.

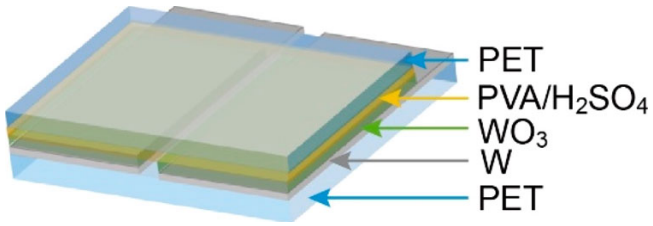

Experimental details. Flexible electrochromic supercapacitor devices were fabricated by assembling two identical F-P cavity-type electrodes on the same plane to serve as working electrodes. Two slim copper conductive adhesives were attached onto the conductive surface of each working electrode. Then, the working electrodes were attached to clean PET sheets using 3M double-sided tape. Subsequently, PVA/H_2SO_4 gel was used to fill the channel between the two working electrodes. The gel served simultaneously as an electrolyte and a separator.

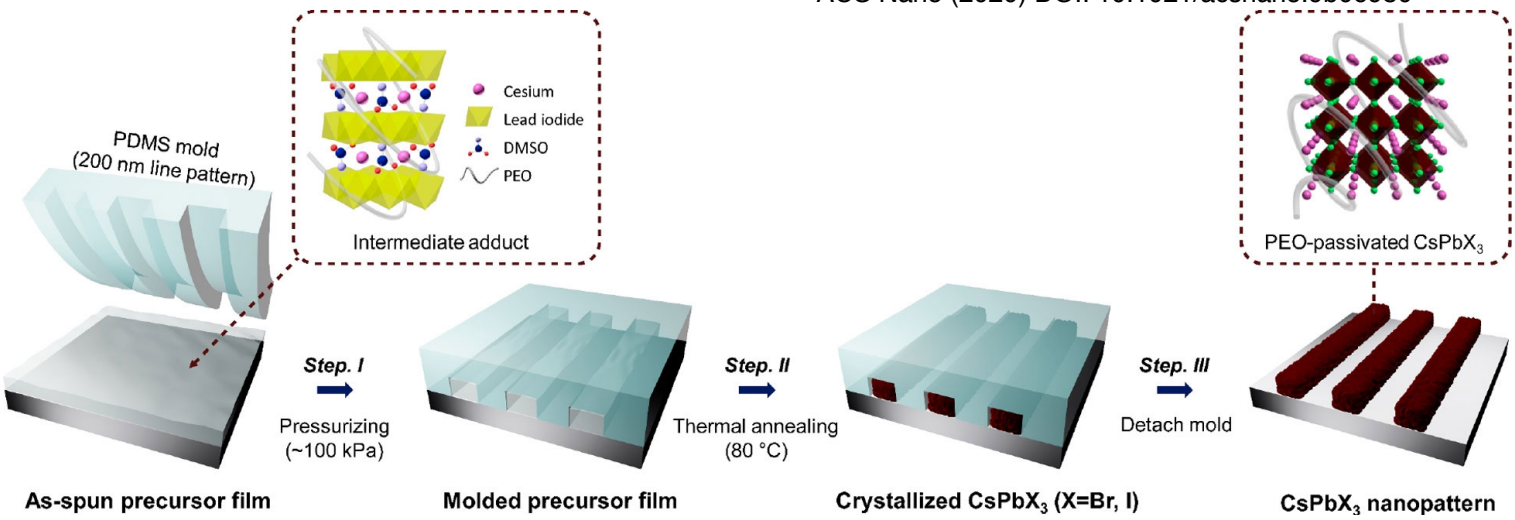

Figure 1. Schematics of the polymer-assisted nanoimprinting with polymer additive (PAN−PA) process. A 1:1 molar ratio of CsBr and $PbBr_2$ or CsI and PbI_2 dissolved in DMSO with polyethylene oxide (PEO) was spin-coated, and the resultant as-spun soft and moldable adduct film was compressed by a prepatterned PDMS mold in conformal contact at ~100 kPa (Step I), followed by thermal annealing at 80 ° C for 15 min (Step II). After removing the mold (Step III), $CsPbX_3$ (X = Br, I) nanopatterns were obtained.

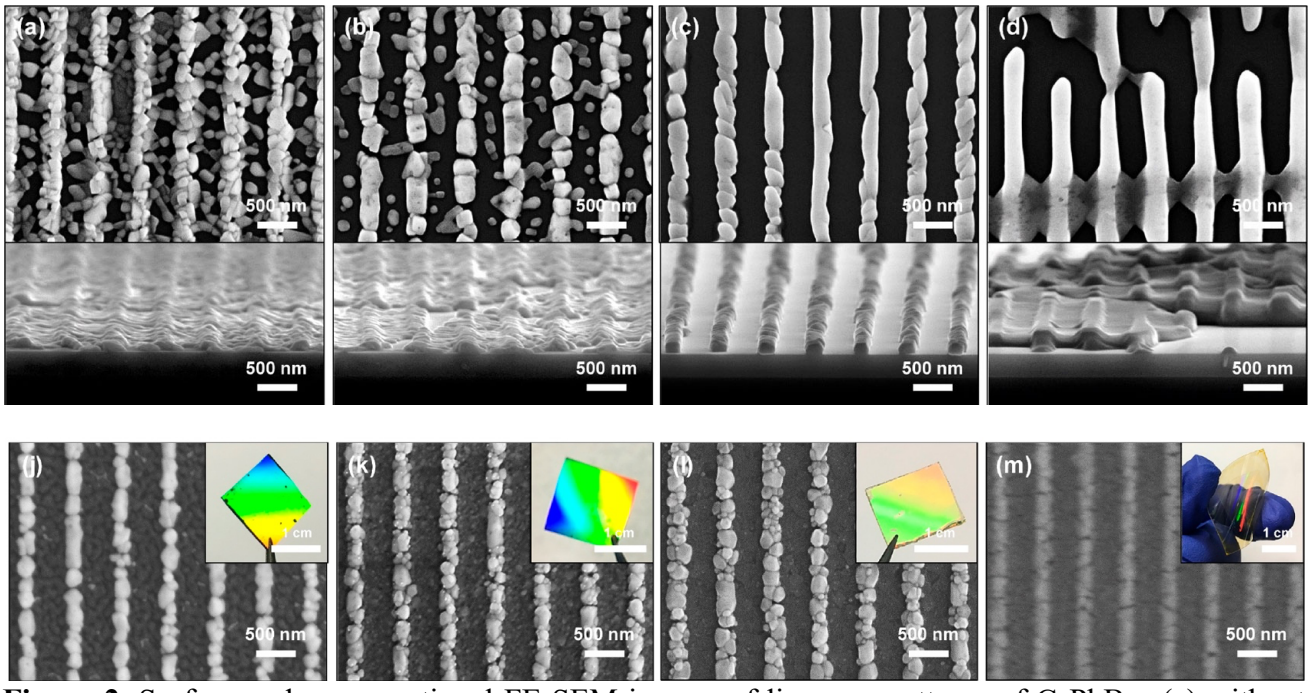

Figure 2. Surface and cross-sectional FE-SEM images of line nanopatterns of $CsPbBr_3$ (a) without PEO and processed by PAN−PA with a weight ratio of (b) 0.5%, (c) 1%, and (d) 3% of PEO with respect to the $CsPbBr_3$ precursor. FE-SEM images of $CsPbBr_3$ nanopatterns processed by PAN−PA on various substrates: (j) Al, (k) Au, (l) ITO, and (m) PET with the surface fringe patterns (inset photographs).

Interpret the figures and text by expanding on what is being illustrated, explaining procedures or techniques, indicating why it might be important or making connections to our class readings and laboratory work. Tell more than rewriting the caption. Try to use your interpretation to demonstrate additional knowledge beyond what is shown here. (**You should write on each page for about 10 minutes**.)

ACS Nano (2019) DOI: 10.1021/acsnano.8b06683

Preparation of SA/PEG-AuNps/EDTA. First, 4.9 g of 2 wt % sodium alginate solution was weighed out, and 0.1 g of $CaCO_3$ was added into it. After the solution was stirred, 0.2 g of D-(+)-gluconic acid δ-lactone was added and the mixture stirred for 10 s. AuNps was prepared by the classic citric acid reduction method: heated 3 mL 0.029 M chloroauric acid in 200 mL ddH_2O to boil (about 160−170 °C) at 450 rpm, then 7 mL 1 wt % trisodium citrate was added and continued to heat for 15 min and stirred for 30 min. Then cool it down to room temperature. After centrifuging at 11000 rpm and removing the supernatant, the solution was washed twice with ddH_2O and finally retained 10 mL as final AuNps solution. 400 μL of AuNp solution was added into 4 mL of PEG 2000 and the solution mixed evenly.

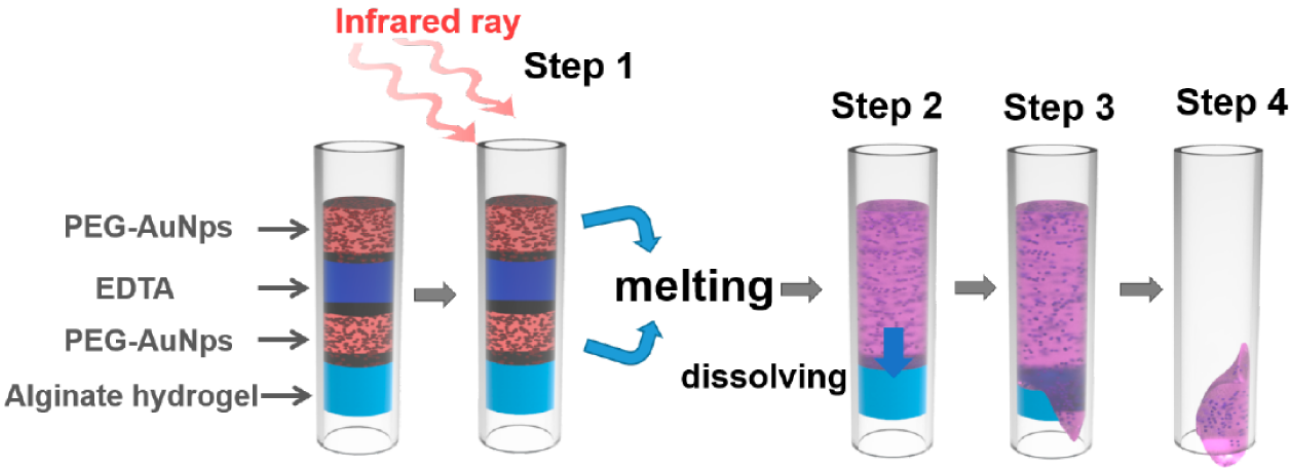

Figure 1. At the beginning, four sections of materials were injected into the tube, respectively. When necessary, near-infrared light was used to illuminate the system to melt the PEGAuNp layers. Then EDTA could mix with PEG-AuNps (step 2) to dissolve the SA gradually (step 3). In the end, the system would be completely unblocked (step 4).

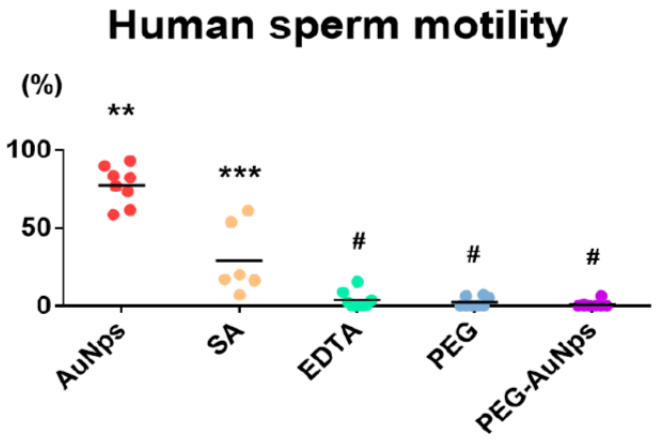

Figure 3. Cytotoxicity of different components to human sperm. After addition of SA, AuNps, EDTA, PEG, and PEG-AuNps, the corresponding cell viability was reduced to 77.38%, 49.11%, 3.95%, 2.38% and 0.97%, respectively.
**, $p < 0.01$; ***, $p < 0.001$; #, $p < 0.0001$

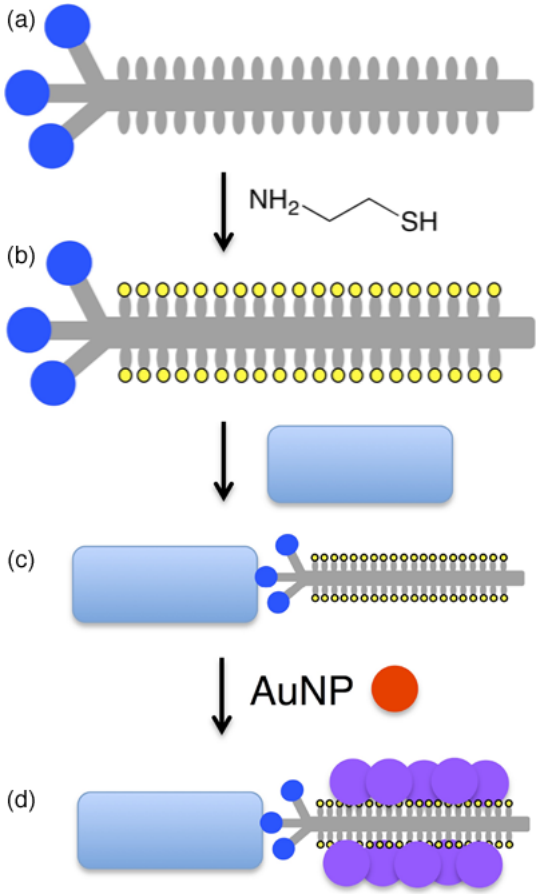

Figure 1. Scheme for phage detection of bacterial species. (a) M13 phage (gray) is engineered to express a foreign receptor binding protein (blue circle) and (b) the phage is thiolated (yellow). (c) Thiolated phages are added to media containing bacteria (blue rectangle) which may attach to the cells. Centrifugation separates cell-phage complexes from free phage. (d) The pellet is resuspended in solution with gold nanoparticles (red), whose aggregation on the thiolated phage produces a color change (purple).

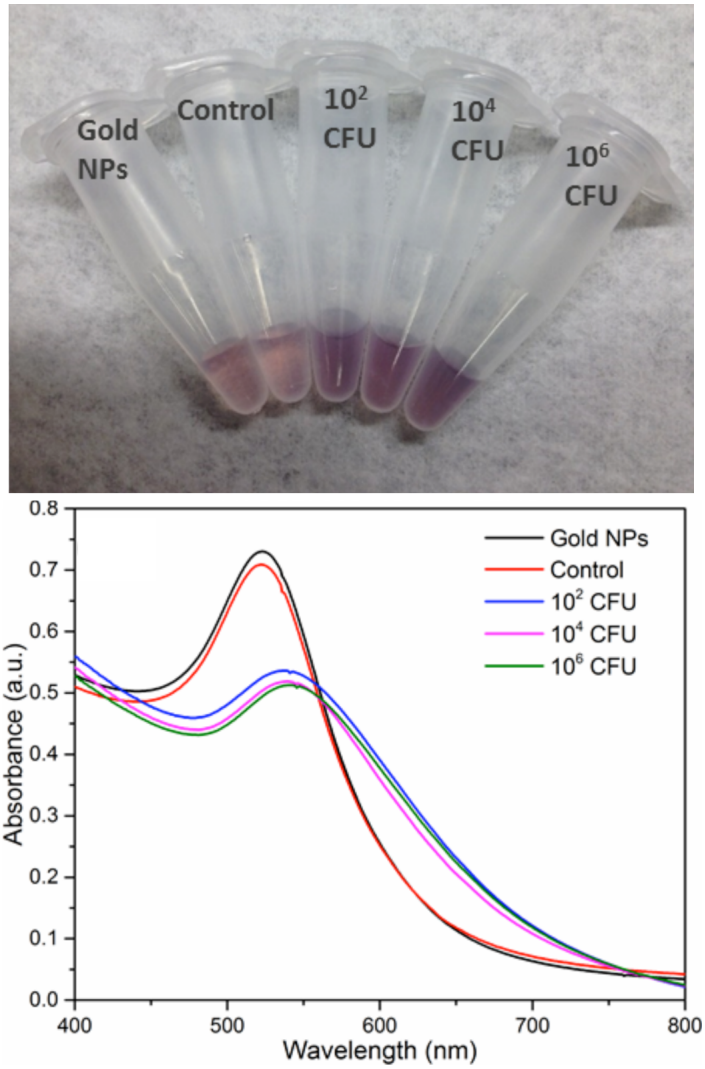

Figure S10. Detection of V. cholerae 0395 with thiolated M13-g3p(CTXφ) in human serum. The amount of bacteria is indicated for each tube and the corresponding spectrum. The control samples are 10^6 CFU host cells incubated with unmodified M13-g3p(CTXφ).

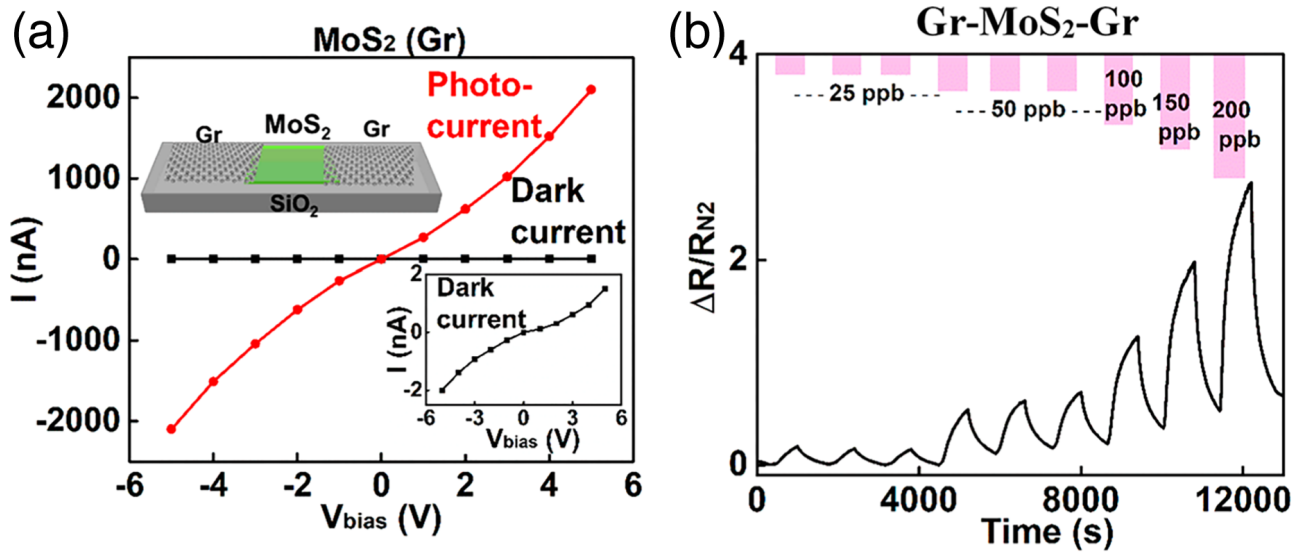

Figure 4. (a) *I*−*V* curves under red LED illumination (red line) and in the dark (black line) of the Gr−MoS_2−Gr device. The inset shows the expanded *I*−*V* curves in the dark. (b) Resistance of a single Gr-MoS_2-Gr sensor to 25 to 200 ppb NO_2 under red LED illumination of incident power of 60.9 nW (light intensity of 60.9 mW/cm^2).

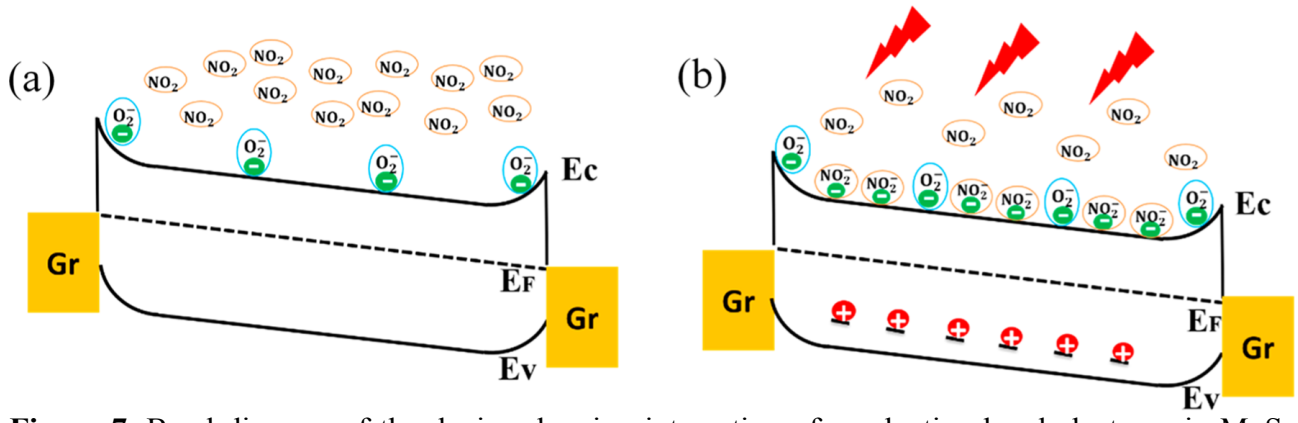

Figure 7. Band diagram of the device showing interaction of conduction band electrons in MoS_2 with NO_2 gas molecules (a) in the dark and (b) under red light illumination. The relatively low sensitivity of the sensor in the dark can be explained by the presence of oxygen which traps the MoS_2 thermally excited electrons. Under red light illumination the population of free electrons increases by several orders of magnitude. These extra electrons are available for interaction with absorbed NO_2 gas molecules which can act as electron acceptors to capture the photoexcited electrons, thus leading to a decrease of current.

Synthesis of GO. GO was synthesized using the Tour method. In a typical synthesis a solution of 360 mL of concentrated sulfuric acid and 40 mL of phosphoric acid was added to 6 g of graphite and 18 g of potassium permanganate. The mixture was heated to 50° C for 12 h. After the reaction had cooled to room temperature, the solution was added to 400 mL of deionized (DI)-water ice and stirred. A total of 4 ml of 30 wt % hydrogen peroxide was added, turning the solution bright yellow. The solution was subsequently passed through a 250 µm sieve. The filtrate is centrifuged 9 times in DI water at 10,000 rpm for 1 h until the pH of the supernatant decanted away is neutral. A final centrifugation step is performed in ethanol. The filtrate is then dried on a hot plate at 50° C, leaving the brown powder as product.

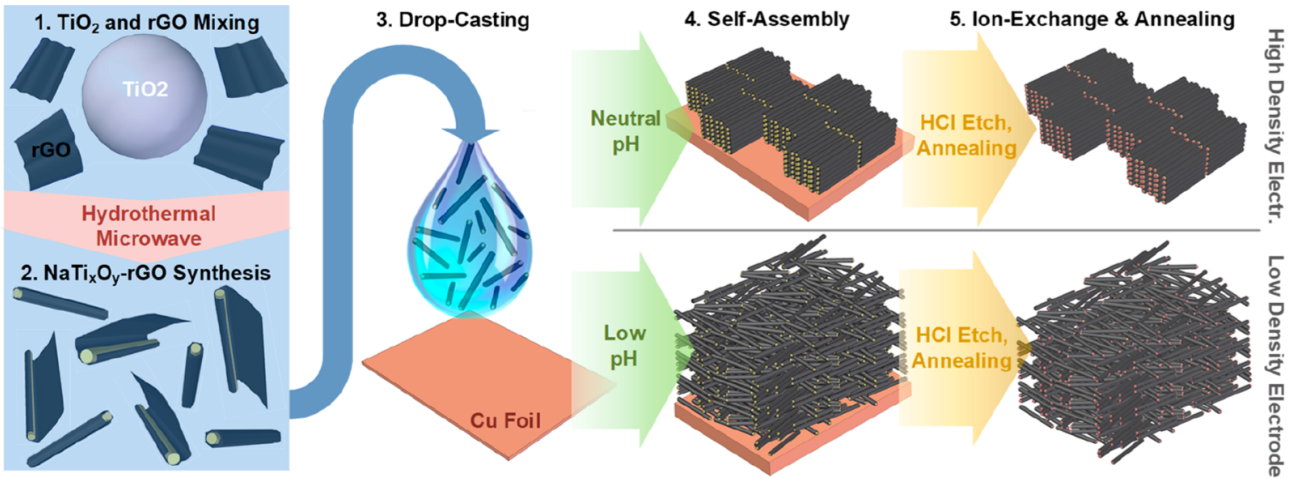

Figure 1. Schematic overview of rGONaTi_xO_y nanorod synthesis and electrode fabrication process.

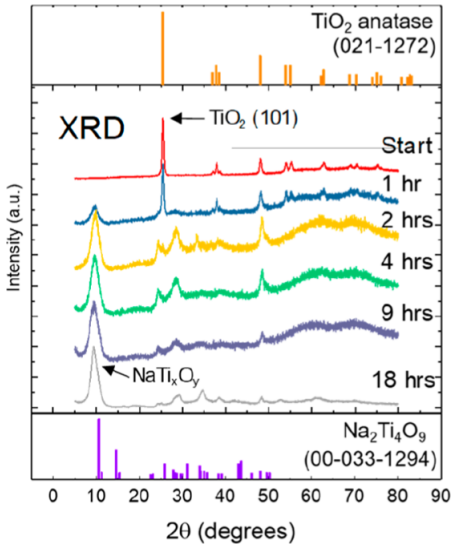

Figure 2. Fabrication of rGONaTi_xO_y nanorods and XRD at different reaction times.

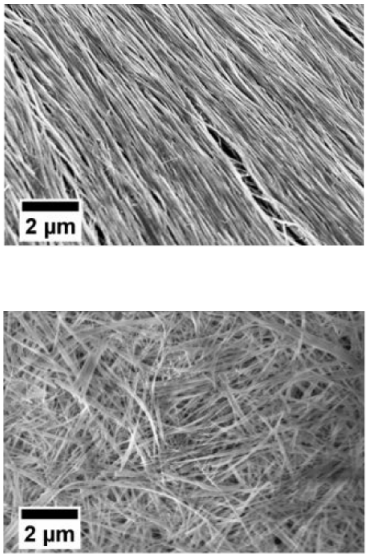

Figure S9. SEM images of aligned and non-aligned rGONaTi_xO_y films.

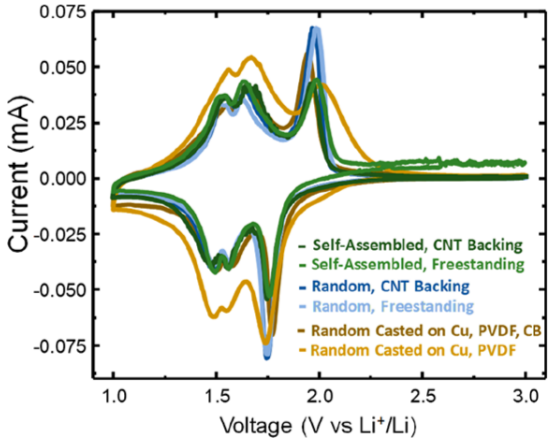

Figure 6. Cyclic voltammogram of rGONaTi_xO_y electrodes at 0.05 C.

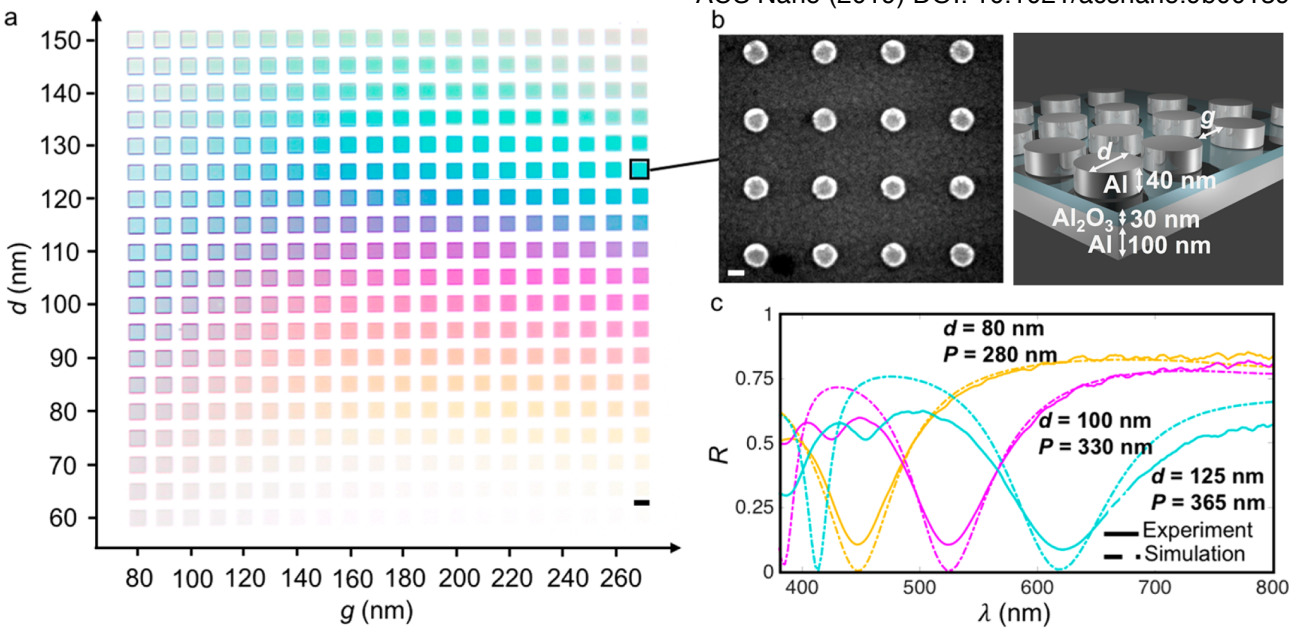

Figure 2. 40 nm thick Al disks whose diameter d is varied along with the gap size between disks g to give the periodicity $P = d + g$. (a) Bright-field optical micrograph of the basic color palette captured by a 20**x** objective lens (NA: 0.45). The gap was varied from 90 nm to 270 nm in increments of 10 nm, and disk diameter ranges from 60 nm to 150 nm in increments of 5 nm. The colors of the bottom two rows are hardly visible, in particular for large pitches, as their resonance is not entirely within the visible range. (b) SEM image for the array with P = 395 nm and d = 125 nm and idealized schematic. (c) Experimental and simulated reflection spectra for disks with d = 80 nm, P = 280 nm; d = 100 nm, P = 330 nm; and d = 125 nm, P = 365 nm.

Chem 150 **First Test** March 7, 2018

Interpret the figures by expanding on what is being illustrated, explaining procedures or techniques, indicating why it might be important or making connections to our class readings and laboratory work. Tell more than rewriting the caption. Try to use your interpretation to demonstrate additional knowledge beyond what is shown here. (**You should write on each page for about 10 minutes**.)

ACS Nano (2018) DOI: 10.1021/acsnano.7b08539

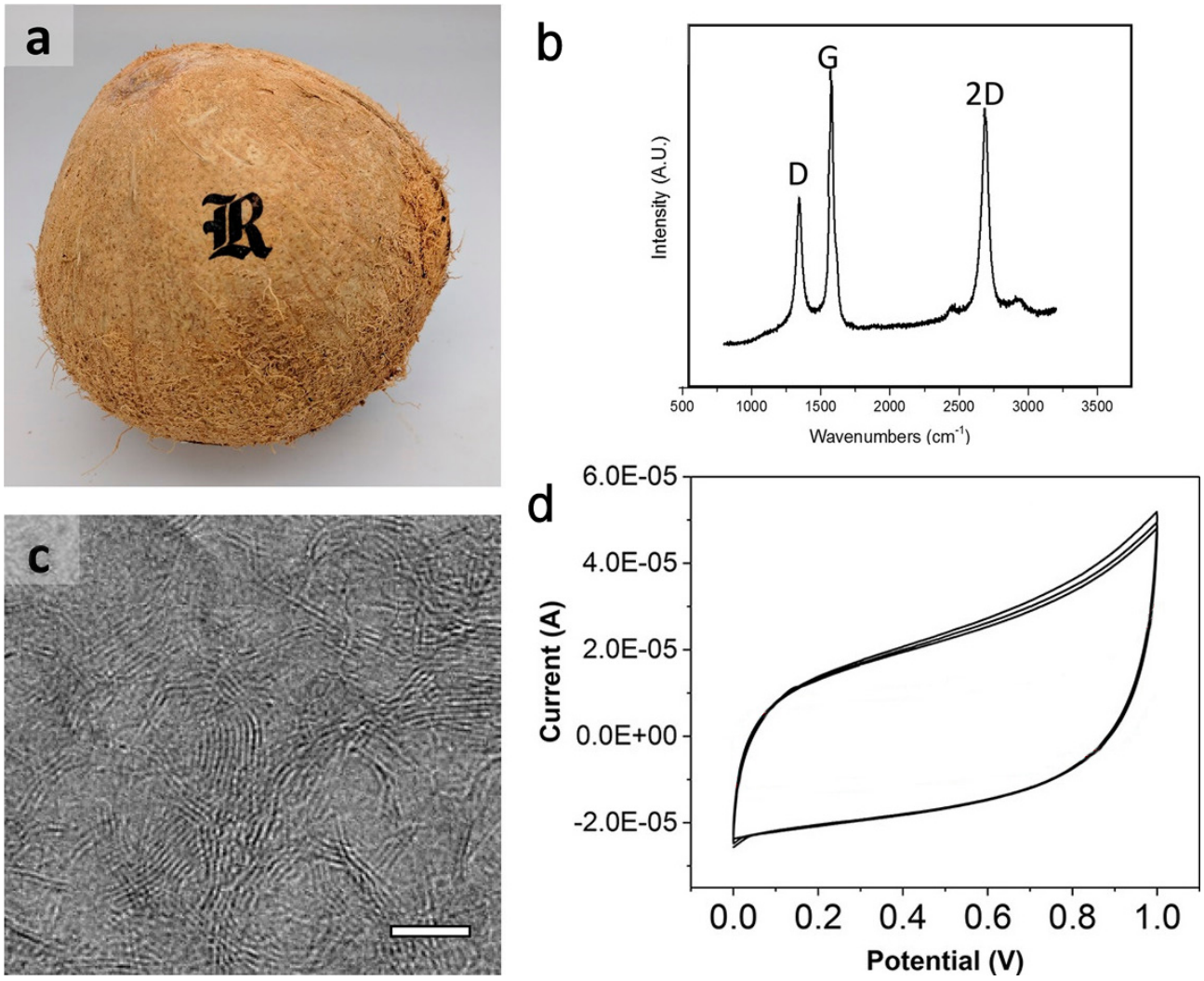

Figure 1. Laser-induced graphene (LIG) involves the conversion of a carbon precursor first to amorphous carbon followed by a conversion to graphene upon subsequent lasing. (a) Picture of LIG patterned into an "R" on a coconut (2 cm tall). (b) Raman spectrum of coconut-derived LIG lased two times at 10% speed and 5% power. (c) High-resolution TEM coconut LIG (10% speed, 5% power, 5x) showing the characteristic 0.34 nm *d*-spacing of graphene. The scale bar is 5 nm. (d) Cyclic voltammogram at 10 mV/s scan rate for a twice-lased coconut. The ability to form LIG on such substrates would potentially allow applications such as flexible micro-supercapacitors on renewable materials or even edible electronics, after a thorough toxicity study.

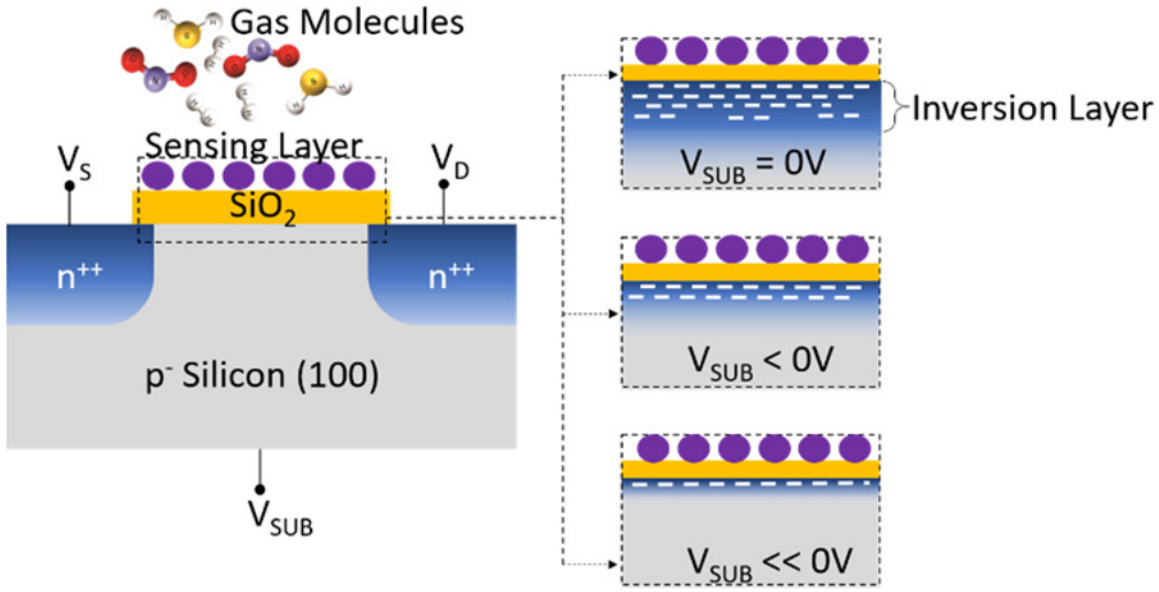

Figure 1. Cross-sectional schematic of a chemically sensitive-FET. Sensing layers composed of Ni (0.3 nm) and Pd (1 nm) are used for H_2 gas sensing, where H_2 readily dissociates over Pd at room temperature into atomic hydrogen, leading to the formation of PdH_x. The *p*-body is lightly doped (~10^{14} boron atoms cm^{-3}) and has a native oxide coating (2.5 to 3 nm). Higher sensitivity is obtained by adjusting $\mathbf{V}_{SUB}$ to control the thickness of the inversion layer.

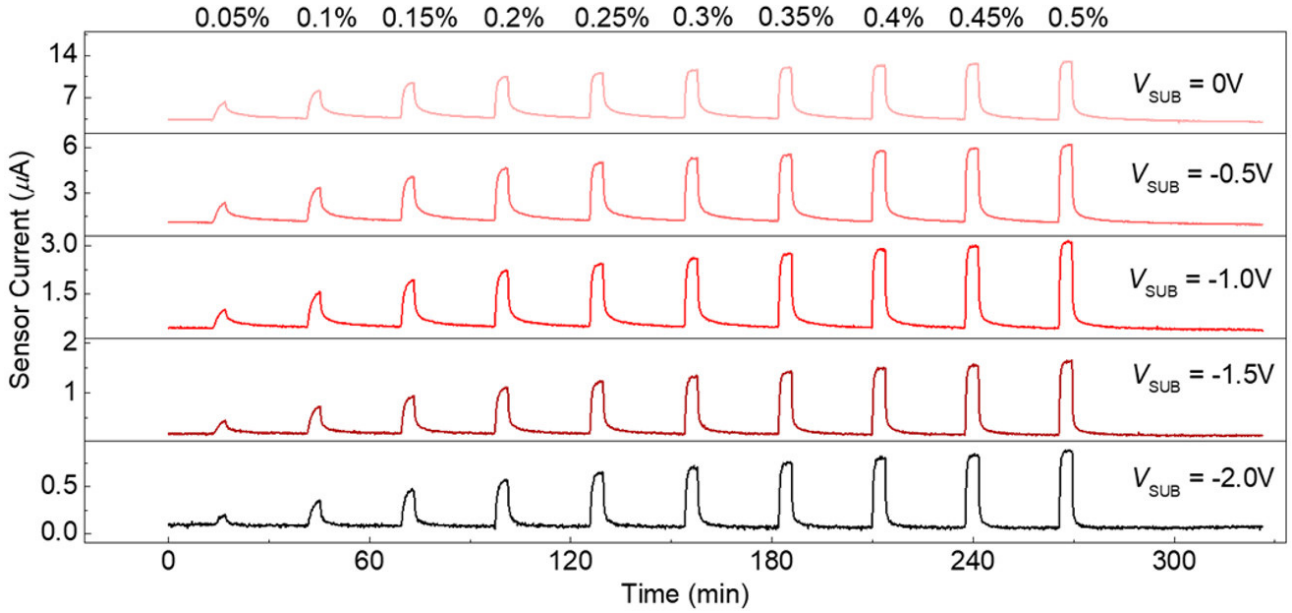

Figure 3. Experimentally measured current of a Ni−Pd CS-FET in response to different H_2 concentrations and at different body biases ($\mathbf{V}_{DS}$ = 3 V).

ACS Nano (2018) DOI: 10.1021/acsnano.7b07739

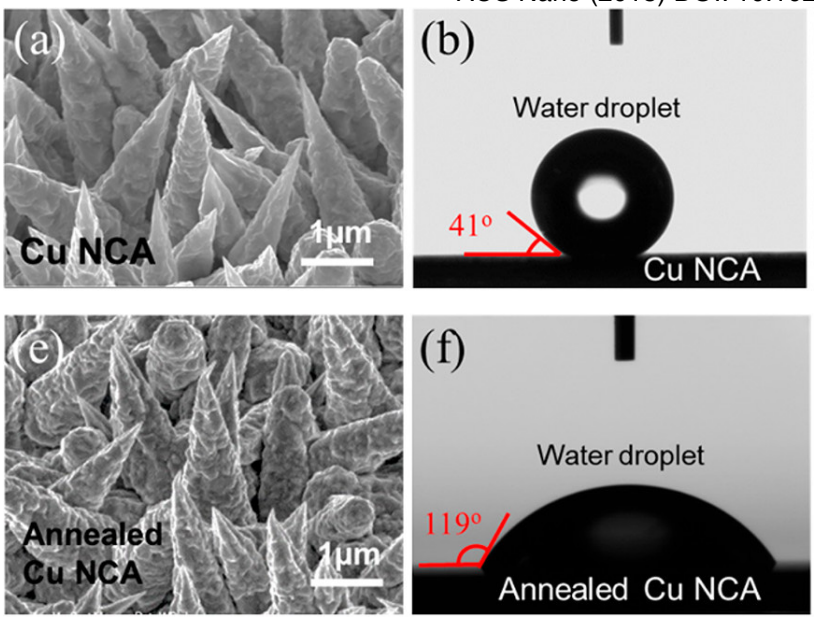

Figure 5. Impact of annealing treatment. (a) SEM image of an as-fabricated Cu nanocone array (NCA) surface. (b) Image of a water droplet on the Cu NCA surface, confirming that it is hydrophobic. The as-fabricated Cu NCA surface is easily oxidized once exposed to air. (e) SEM image of an annealed Cu NCA surface. (f) Image of a water droplet on the annealed Cu NCA substrate indicating that it is hydrophilic.

Nanoletters (2018) DOI: 10.1021/acs.nanolett.7b01870

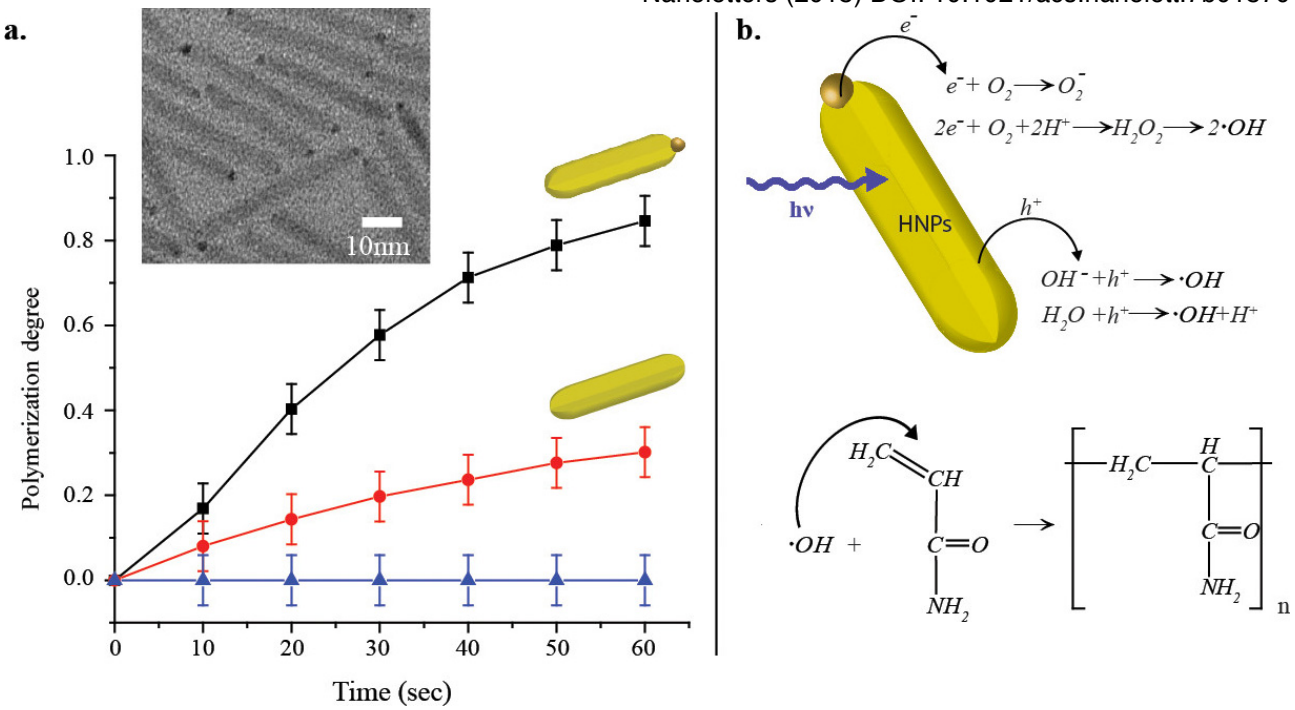

Figure 1. Acrylamide polymerization. (a) Polymerization degree under UV light at 385 nm with intensity of 20 mW/cm^2 using CdS−Au (top, black), CdS (middle, red), and 2-hydroxy-4′-(2-hydroxyethoxy)-2-methylpropiophenone (bottom, blue) as photoinitiators. The polymerization degree of acrylamide was calculated from the decrease of the FTIR absorption peaks of methylene group vibrations at 988 cm^{-1} (assigned to the out-of-plane bending mode of the =C−H unit) normalized to the C=O stretch peak at 1654 cm^{-1} as an internal standard. Inset: TEM image of CdS−Au having rod dimensions of 37 x 4 nm with 1.5 nm diameter Au tip. (b) A scheme of the photocatalytic polymerization.

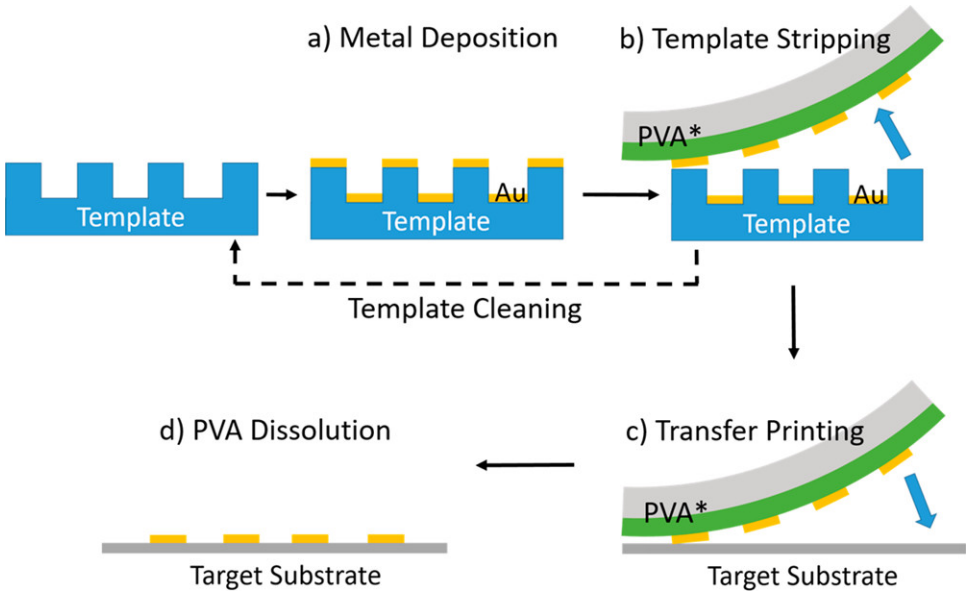

Figure 1. The process flow of template-stripping based nanotransfer printing (a) Au is evaporated onto a silicon template by e-beam evaporation. (b) The topmost layer is stripped by an adhesive supported PVA sheet (PVA*) and (c) is then transferred onto the target surface by lamination. (d) Subsequently, the support is peeled off and the PVA is simply dissolved in water. The template can be reused after etching away the remaining gold. In our method, no adhesion layer is required to improve the adhesion between glass and gold, which enables faster and cheaper processing. This observed strong adhesion and stability was tested by means of tape peeling tests, ultrasound, and temperature shocks.

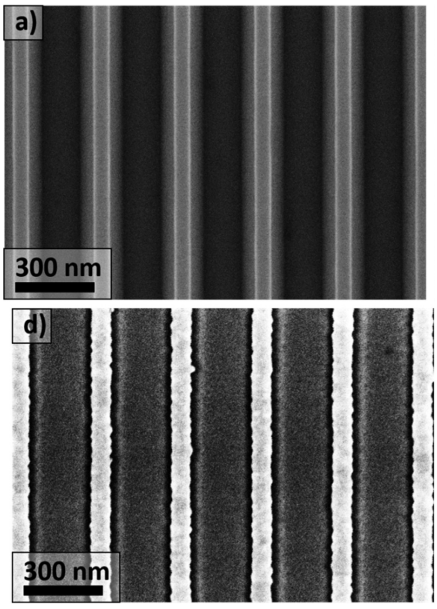

Figure 2. SEM images of a template and the transferred nanostructures. The widths of the nanowires are 65 nm with a pitch of 300 nm. (a) Intact silicon template after 50 transfer cycles. (d) Transferred 20 nm thick gold pattern on a glass substrate.

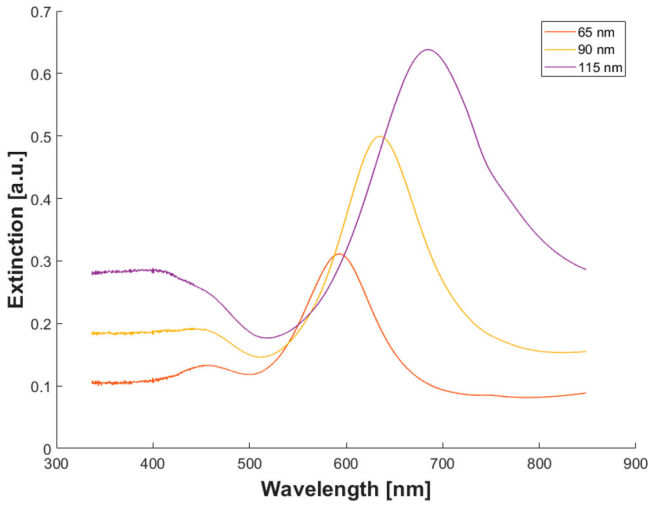

Figure 4. Spectrophotometry of transferred ordered 10 nm thick nanowire arrays on glass with a pitch of 300 nm. The widths of the nanowires are 65, 90, and 115 nm. The spectral full width at half-maximum (fwhm) is 83, 91, and 127 nm for the different line widths.

Chem 150 **First Test** March 1, 2017

Interpret the figures by expanding on what is being illustrated, explaining procedures or techniques, indicating why it might be important or making connections to our class readings and laboratory work. Tell more than rewriting the caption. Try to use your interpretation to demonstrate additional knowledge beyond what is shown here. (You should write for about 10 minutes on each page.)

Nano Lett (2017) DOI: 10.1021/acs.nanolett.6b04071

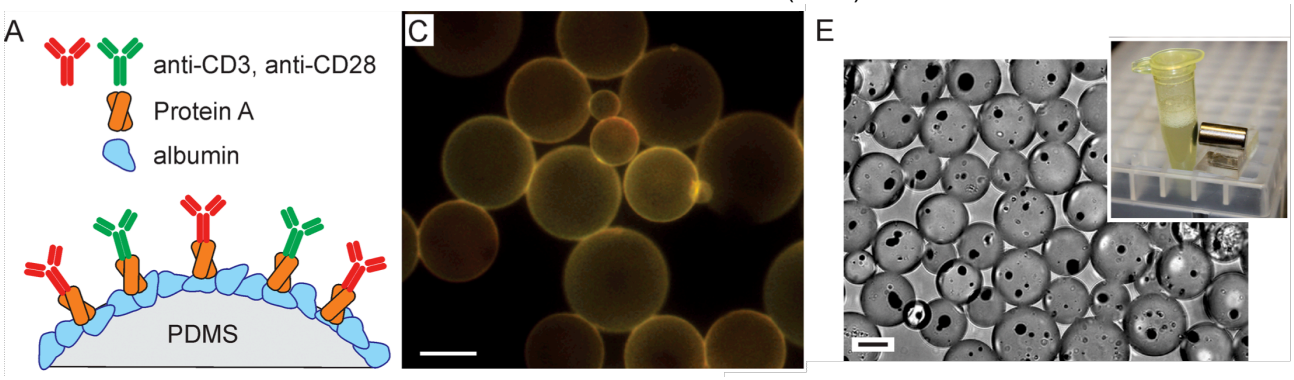

Figure 1. PDMS prepolymer was dispersed by agitation into small particles into an aqueous phase using human serum albumin as the surfactant to stabilize the individual droplets during a subsequent curing phase. (A) Molecular strategy for attaching anti-CD3 and anti-CD28 to PDMS beads. (C) Sylgard 184 beads, illustrating morphology and size distribution. PDMS was stained with Nile Red (red), and anti-CD3 was labeled with Alexa 488 (green.) Scale bar: 25 μm. (E) Incorporation of magnetic particles into PDMS beads allow collection.

ACS Nano (2017) DOI: 10.1021/acsnano.6b07960

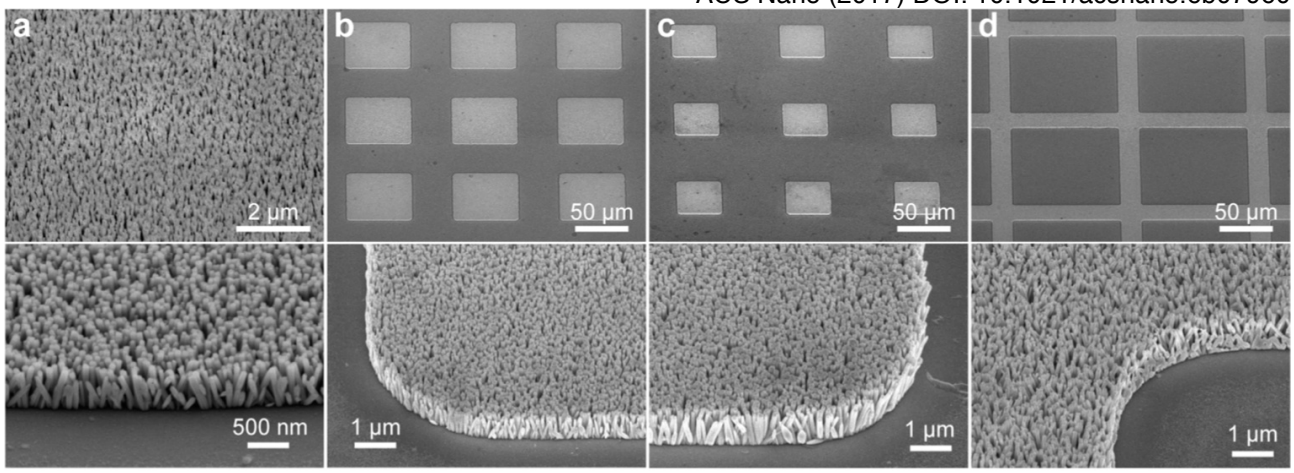

Figure 2. SEM images of four samples with different n-ZnO nanowire array patterns grown on Si through photolithography and low temperature hydrothermal reaction. The ZnO seed layer was deposited by radio frequency (RF) magnetron sputtering at room temperature. A lithography process was used for different patterns to provide for the upcoming nanowire growth. A SUN-9i negative photoresist was first spin-coated on the ZnO seed layer and then processed in turn with prebaking (110 °C, 90 s), exposure (5 s), postbaking (135 °C, 60 s), and development (30 s). Then, all the samples were placed into a mixed nutrient solutions (30 mM $Zn(NO_3)_2$ and 30 mM hexamethylenetetramine (HMTA)) at 80 °C for 3 h for the growth of ZnO nanowire arrays.

Synthesis of NPs of PB. Two aqueous solutions were first prepared separately in 20 mL of distilled water, with one containing 0.2 mmol of $K_4[Fe(CN)_6]$ and 5 mmol of citric acid and the other containing 0.2 mmol of $FeCl_3$ and 5 mmol of citric acid. These two aqueous solutions were mixed at room temperature under magnetic stirring. After reaction for 30 min, blue precipitates were obtained upon adding acetone and centrifuging at 11000 rpm for 10 minutes.

Color switching reaction. In a typical fabrication of solid films for color switching system, TiO_2/H_2O dispersion (800 µl), PB/H_2O dispersion (200 µl), hydroxyethyl cellulose/H_2O stock solution (33.3 mg ml^{-1}, 200 µl), and ethylene glycol, (800 µl) were mixed together and sonicated to form a homogenous solution. The solution was drop cast directly on a glass substrate, and then dried in an oven at 80 °C for 12 h to form a solid film. The solid film was further annealed at 120 °C for 30 minutes. Photoirradiation was performed using a typical laboratory 365-nm UV lamp (8 W, Spectroline EN-180). The UV-Vis absorption spectra of the solid film were measured by UV-Vis spectrophotometer (HR2000CG-UV-NIR, Ocean Optics).

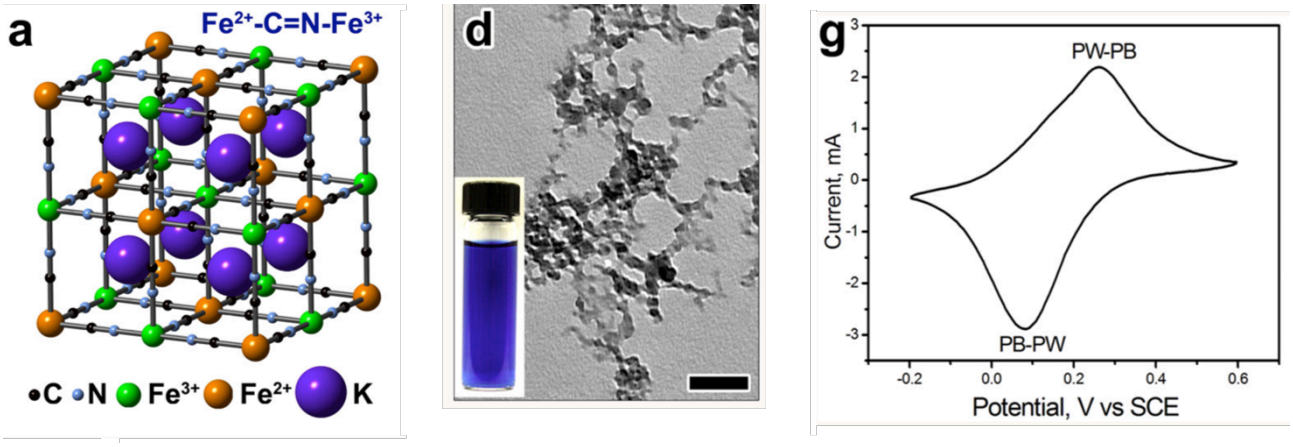

Figure 1. (a) Schematic illustration of a face-centered cubic structure of PB. Owing to the lengthy C≡N bonds, subunit cells contain large interstitial sites for cations such as K^+. (d) TEM image of PB. Scale bar: 100 nm. Inset: digital photograph of aqueous dispersion of PB. (g) Cyclic voltammogram of PB NPs on FTO in 0.1 M KCl solution at a scanning rate of 5 mV s^{-1}.

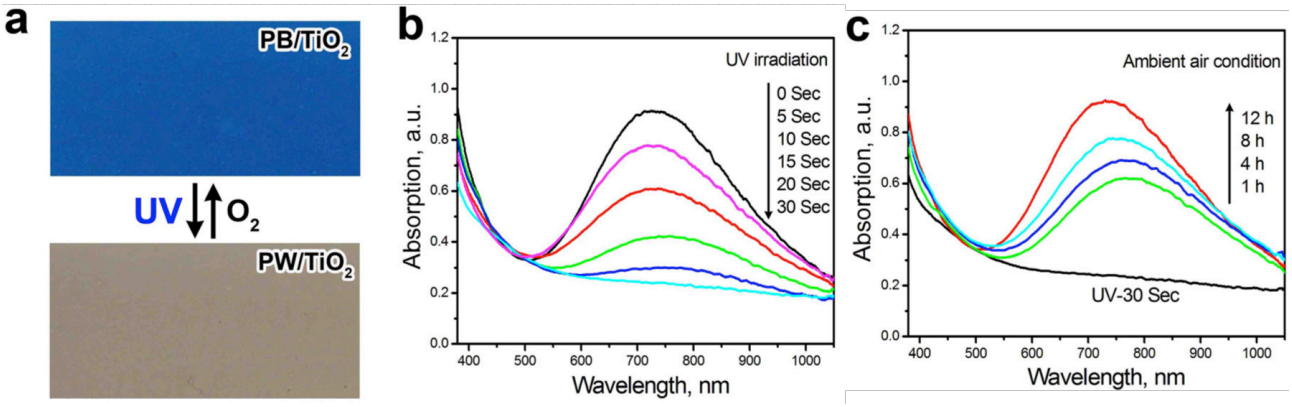

Figure 2. Photoreversible color switching and stability of the PB/TiO_2 solid film. (a) Digital images of a solid film showing the decoloration and recoloration process; (b) UV−vis spectra showing the decoloration process under UV irradiation; (c) UV−vis spectra showing the recoloration process at room temperature under ambient air.

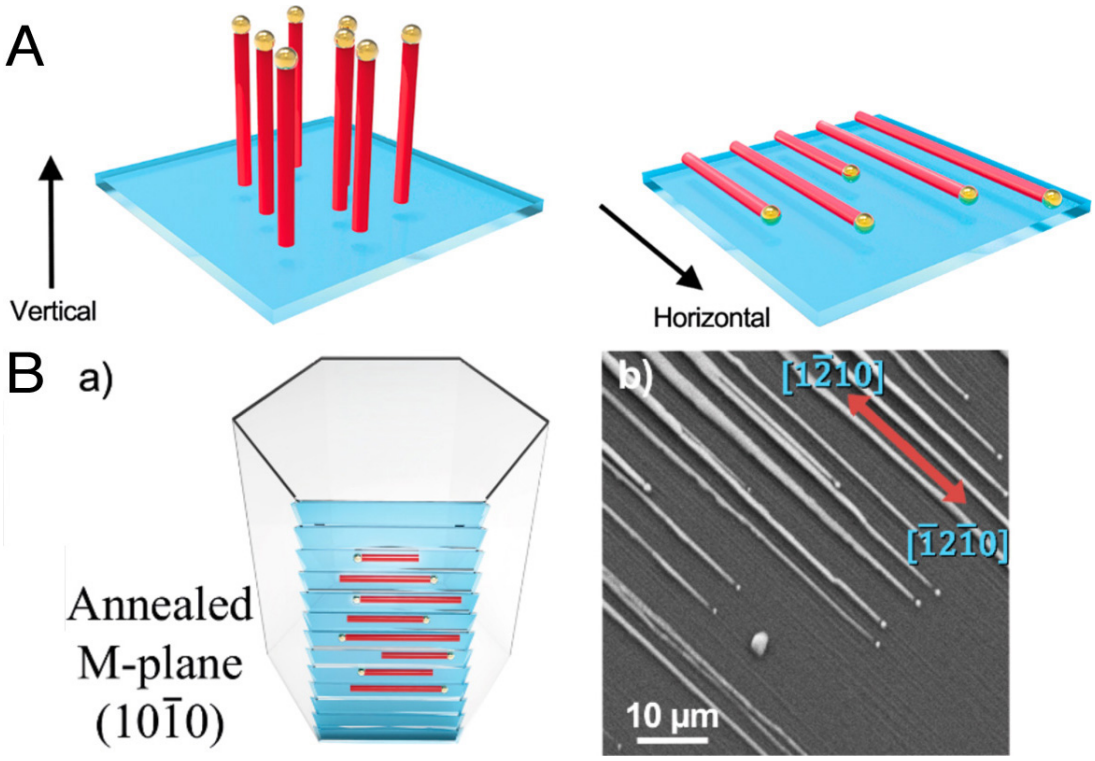

Figure 1. (A) Schematic illustration of vertical VLS growth (left) *vs* guided horizontal growth (right). (B) Graphoepitaxial guided growth of CdSe NWs on a faceted sapphire substrate. (a) schematic illustration of the directional growth; (b) SEM image of the guided CdSe NWs;

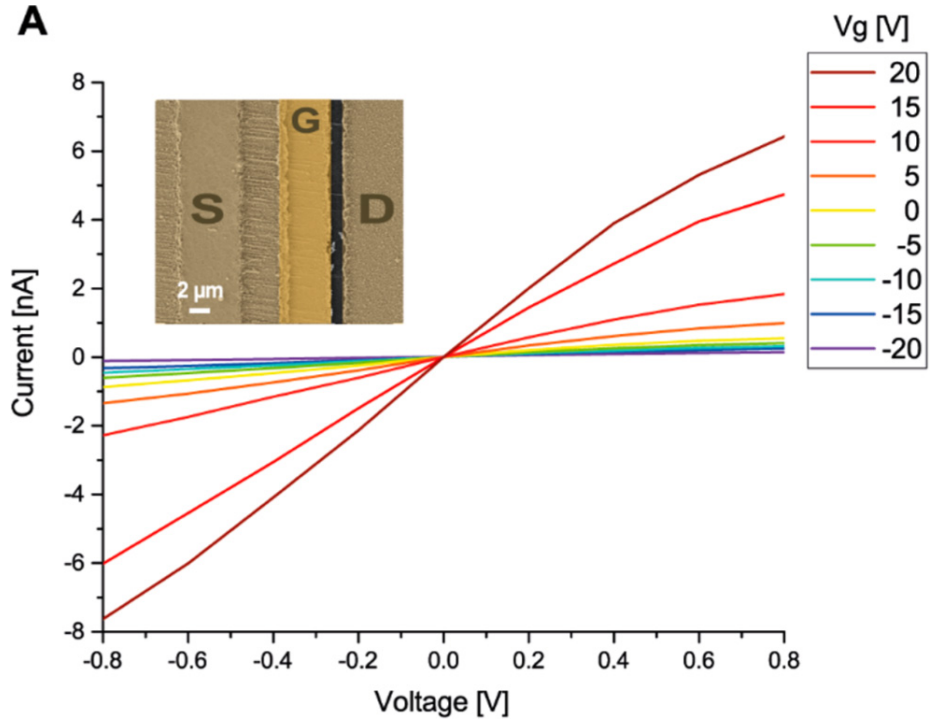

Figure 4. Performance of a typical field-effect transistor based on CdSe NWs. (A) I_{SD} *vs* V_{SD} at different gate voltages. Inset: SEM image of NWs based FET; electrodes are colored and marked.

Synthesis of hollow SnO_2 template: Urea (0.48 g) and $K_2SnO_3 \cdot 3H_2O$ (0.384g) were dissolved in a mixture of ethanol and distilled water and transferred into a Teflon-lined autoclave, which was maintained at 190 °C for 15 h. After this hydrothermal treatment, these SnO_2 particles were collected and washed with ethanol and distilled water, and dried under vacuum.

Synthesis of Sn@C yolk-shell precursor: 0.17 g of the as-synthesized SnO_2 template and 0.68 g glucose were hydrothermally treated at 190 ºC for 10 h, and subsequently annealed at 650 ºC in an H_2/Ar flow for 6 h.

Synthesis of hollow Sb@C yolk-shell product: 0.1 g Sn@C precursor particles and 1.5 g $SbCl_3$ were added into ethanol solution and kept stirring for 30 min. Then the dispersion was transferred into a Teflon-lined autoclave at 80 °C for 24 h. The finally obtained black Sb@C particles were collected and washed with distilled water and ethanol and dried under vacuum.

Characterization. The collected products were characterized by X-ray diffractometry (XRD) using a Rigaku-DMax 2400 diffractometer equipped with the graphite monochromatized Cu Kα radiation at a scanning rate of 0.02° s^{-1}.

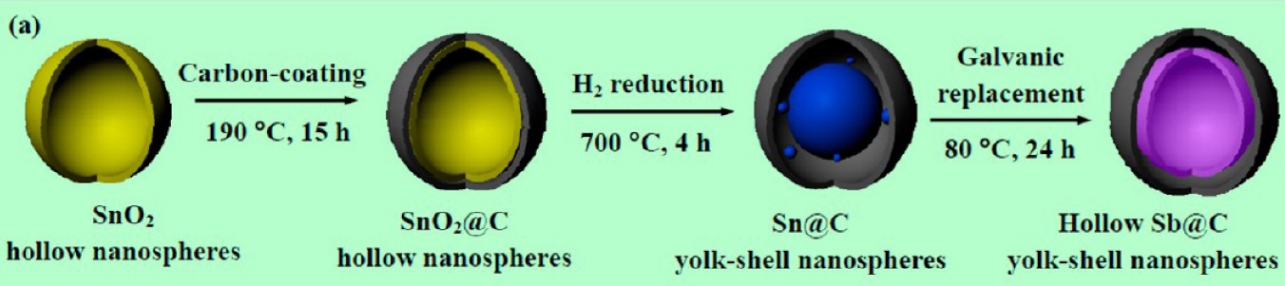

Scheme 1. Schematic evolution of hollow Sb@C yolk−shell nanospheres for Li/Na-ion batteries based on the Kirkendall effect.

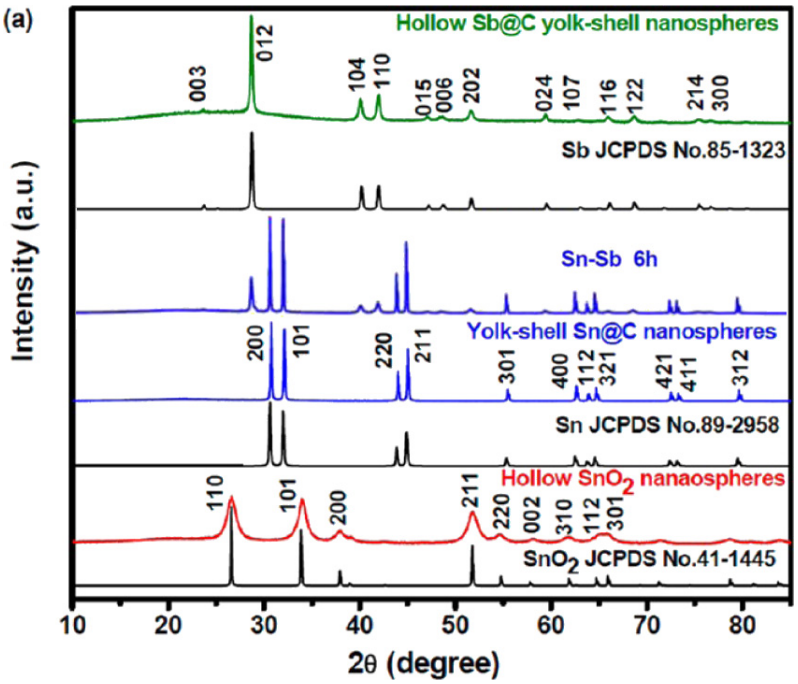

Figure 4. Composition characterizations of hollow Sb@C yolk−shell particles. (a) XRD patterns of SnO_2 template (black), Sn@C precursor (blue), and the as-obtained Sb@C product (green) clearly show that the initially used SnO_2 was first converted into Sn and finally into Sb via the nanoconfined galvanic replacement route.

Interpret the figures by expanding on what is being illustrated, explaining procedures or techniques, indicating why it might be important or making connections to our class readings and laboratory work. Tell more than rewriting the caption. Try to use your interpretation to demonstrate additional knowledge beyond what is shown here. ***All the figures on a given page are from the same paper.***

Nature Energy (2016) 10.1038/nenergy.2015.9

Methods: To make graphene-coated spiky nickel nanoparticles (GrNi), ~5 g of spiky Ni particles (Novamet) were dispersed in 150ml of triethylene glycol (TEG, Sigma Aldrich) and 500 µl of 50% w/w aqueous NaOH solution. After stirring at 185 °C for 8 h, the spiky Ni was collected by centrifugation and washed three times with ethanol. The NaOH solution facilitates decomposition of the organic solvent (TEG), allowing carbon atoms to diffuse into the Ni layer and adhere to the surface. This primes the spiky Ni for low-temperature graphene growth. Samples were then dried in a vacuum oven at 50 °C for 1 h. The dried particles were placed in a tube furnace with the following temperature profile: heating to 100°C at 2°C min^{-1}; heating to 600°C at 20°C min^{-1}; holding temperature at 600°C for 1 h. An Ar flow rate of 80 sccm was maintained throughout the ambient pressure annealing process.

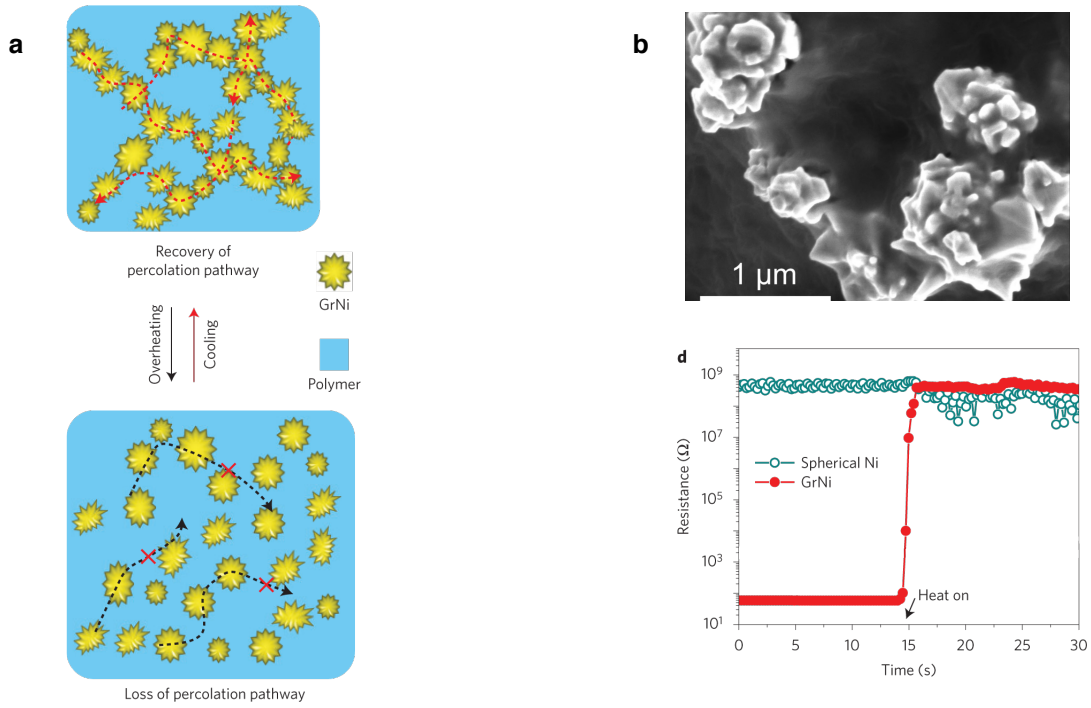

Figure. (a) Thermal switching mechanism of the TRPS material consisting of electrochemically stable GrNi mixed in a polymer matrix with a high thermal expansion coefficient. The polymer composite film has a high electrical conductivity at room temperature due to the quantum tunnelling effect enabled by the GrNi. On heating, the polymer matrix expands, thus separating the conductive particles, which can decrease the value of σ by a factor of 10^7–10^8. On cooling, the polymer shrinks and regains the original conductive pathways. (b) SEM image of the PE/GrNi-based TRPS composite showing the GrNi network embedded in the PE matrix. (d) Dependence of resistance on time for PE-based composites with different conductive fillers on heating. The resistance of PE/GrNi increased by 10^8 in <1 s.

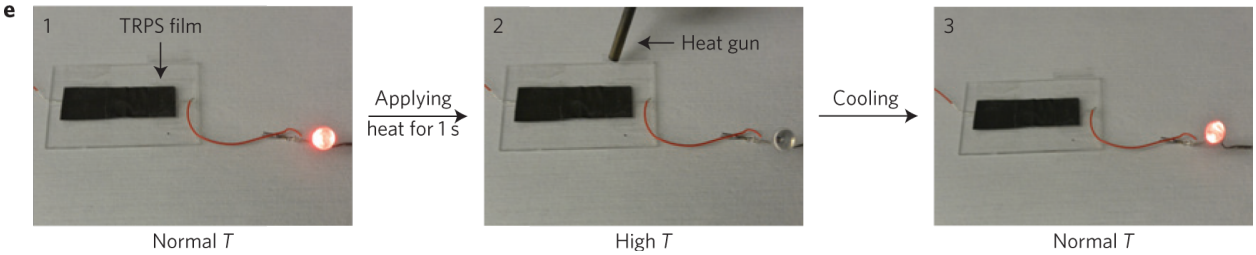

Figure. (e) Demonstration of thermal switching behaviour of a TRPS film using a LED connected in the circuit.

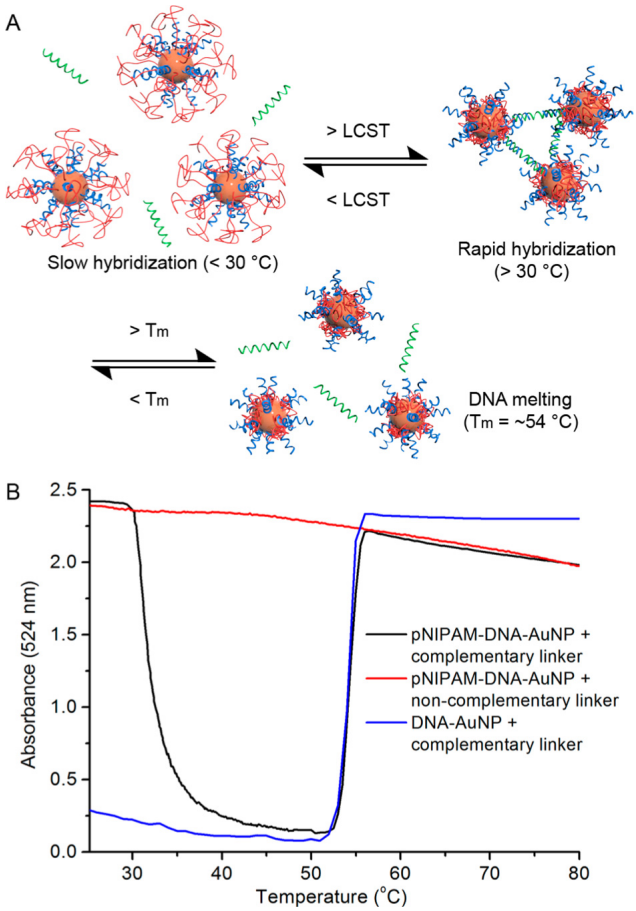

Figure 2. (A) Divalent linker DNA strand (sequence: 5′-CTC CTT ACC CTC ACT AAC CTT TCC-3′) hybridizes with DNA-AuNPs (sequence: 5′-GAG GGT AAG GAG-SH-3′ or 5′-HS-GGA AAG GTT AGT-3′) when the temperature is raised above the LCST of poly(*N*-isopropylacrylamide) (pNIPAM), causing AuNP assembly. A further increase in temperature leads to the melting of double-stranded DNA and redispersion of the aggregates. (B) UV−vis temperature scan is performed at 0.5 °C/min, monitoring AuNP absorption at 524 nm.

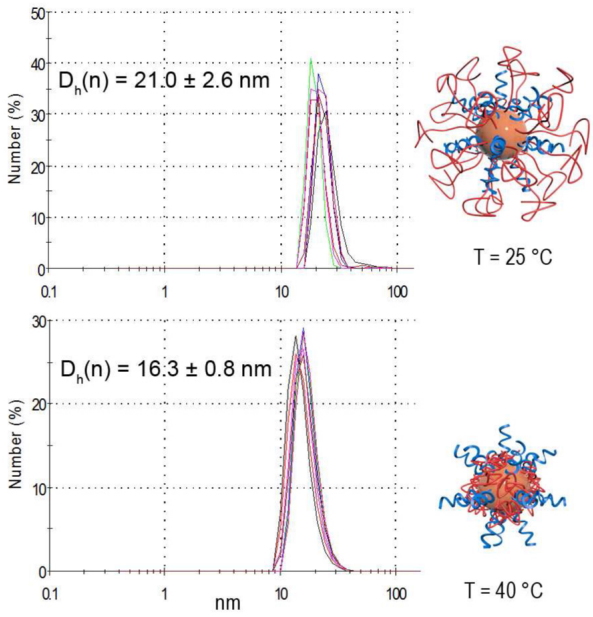

Figure S2. Dynamic light scattering (DLS) measurements of number-averaged hydrodynamic diameters of AuNPs modified with DNA and pNIPAM (molar ratio 1.1:1, 10 kDa pNIPAM) at 25 °C and 40 °C.

Methods: MnSi NWs with a native oxide layer were synthesized on Si(100) substrates. The substrates were placed in the downstream zone in a conventional two-zone horizontal furnace. Anhydrous $MnCl_2$ precursor (0.05 g, 99.999%, Sigma-Aldrich) was placed in an alumina boat in the upstream zone. The temperatures of the two zones were independently controlled. The system was purged with Ar gas for 30 min before each reaction for an inert atmosphere. The Ar gas transported precursor vapor produced at 800 °C to the downstream zone at 950 °C, where $MnCl_2$ decomposed and reacted with the Si substrate to form free-standing MnSi NWs. The reaction time was about 5 min.

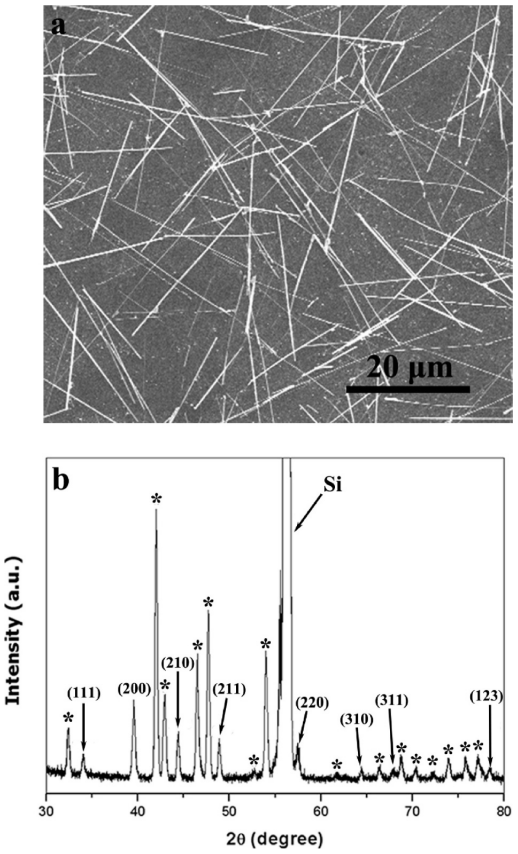

Figure 1. (a) Representative SEM image of MnSi NWs. (b) XRD pattern of the MnSi NWs on silicon substrate. The asterisks in panel b indicate the peaks from $MnSi_{1.7}$ film formed on the Si substrate before the growth of MnSi NWs.

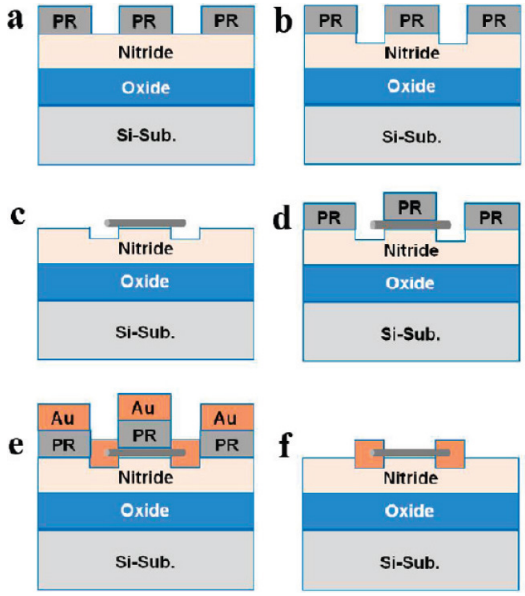

Figure 6. Schematic illustrations (cross-section view) for the fabrication process of a single MnSi NW device. To block Au diffusion and isolate the NW from the substrate, nitride and oxide layers were initially deposited on the silicon substrate followed by photoresist patterning as shown in panel a. The nitride layer was etched by 50% diluted HF solution for 50 s with a 12 nm/min etch rate (panel b). After removing the photoresist a MnSi NW was positioned by a nanomanipulator between two pad areas (panel c). The photoresist was patterned again (panel d), and Au was evaporated on top of the wafer (panel e). Finally, the photoresist was lifted off in an acetone solvent (panel f).

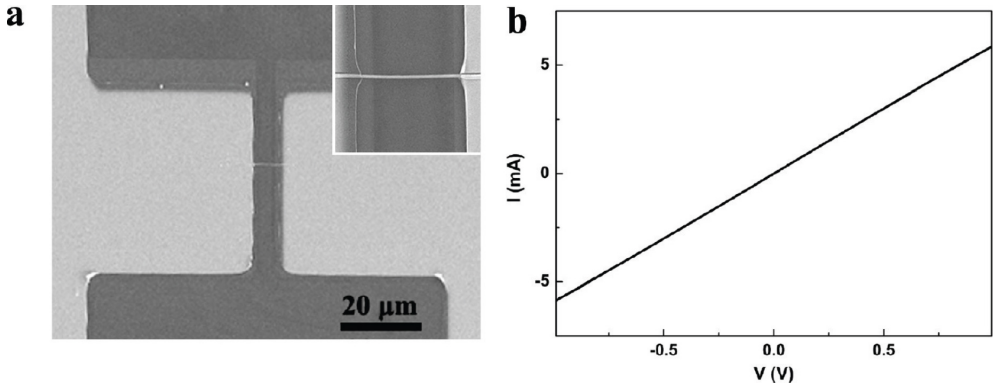

Figure 7. Electrical properties of an individual MnSi NW. (a) SEM image of the MnSi NW device. Inset shows a magnified SEM image of the MnSi NW lying between the Au electrodes. (b) *I-V* curve recorded on the MnSi NW device by two-probe measurement.

We have successfully fabricated Cu_2O nanowire array photocathodes for hydrogen generation from solar water splitting delivering unprecedentedly high photocurrent densities of 10 mA cm^{-2} and stable operation beyond 50 h, establishing a new benchmark for metal oxide based photoelectrodes.

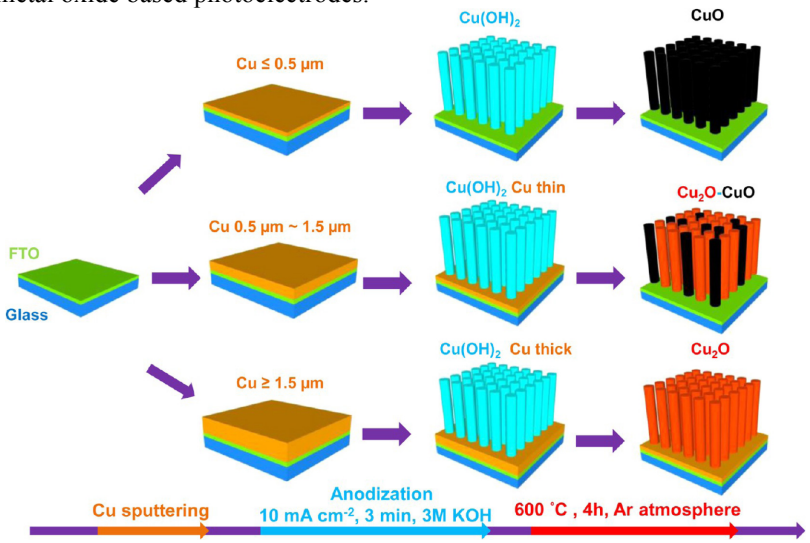

Figure 1. Schematic diagram of phase controlled synthesis of copper oxide nanowire arrays. Copper oxide nanostructures are synthesized from Cu thin films on FTO/glass by a two-step process. Cu films are first anodized to form $Cu(OH)_2$ nanowires, and subsequent annealing in Ar leads to dehydration and formation of oxide phases. For a fixed anodization treatment, the starting thicknesses of Cu ultimately dictate whether pure CuO, mixed Cu_2O–CuO, or pure Cu_2O nanowires are formed.

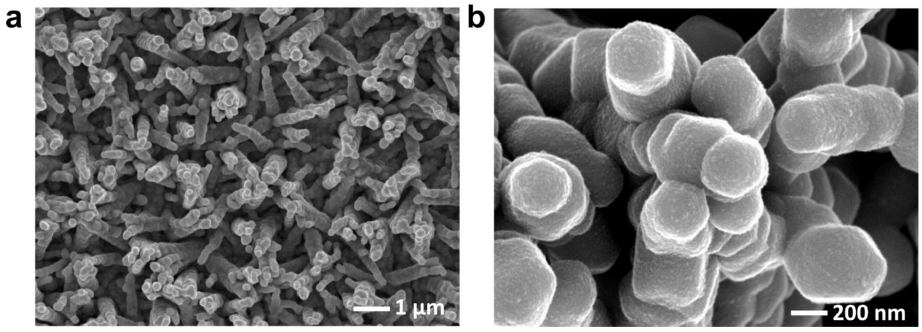

Figure 4. SEM characterization. (a) A Cu_2O NW following ALD overlayer deposition of aluminum-doped zinc oxide and TiO_2. (b) Top view SEM image of complete Cu_2O NW device following electrodeposition of RuO_x catalyst.

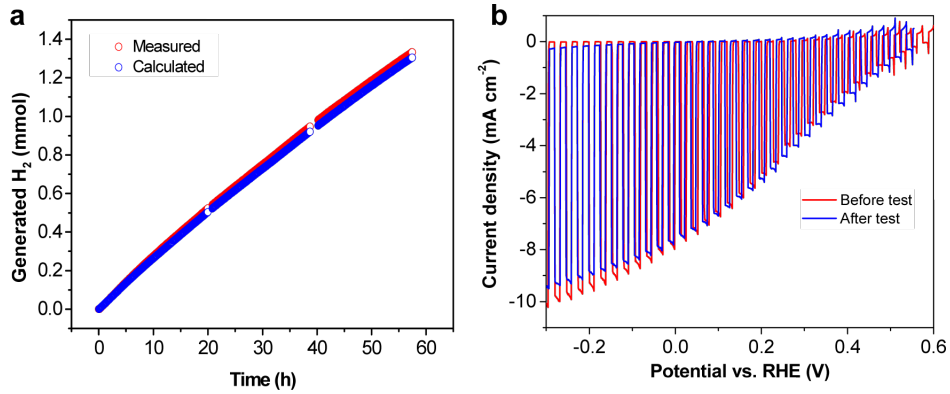

Figure S9. The NW array photocathode showed a constant Faradaic efficiency of ~100% toward hydrogen evolution. (a) The amount of hydrogen produced during stability test. (b) J-V curves of Cu_2O NW devices before and after 57 h stability measurement. Samples tested in pH 5 electrolyte and under chopped simulated AM 1.5G illumination.

Chem 150 **First Test** March 5, 2014

Interpret the figures by expanding on what is being illustrated, explaining procedures or techniques, indicating why it might be important or making connections to our class readings and laboratory work. Tell more than rewriting the caption. Try to use your interpretation to demonstrate additional knowledge beyond what is shown here. ***All the figures on a given page are from the same paper.***

Nano Lett. (2014) dx.doi.org/10.1021/nl404281h

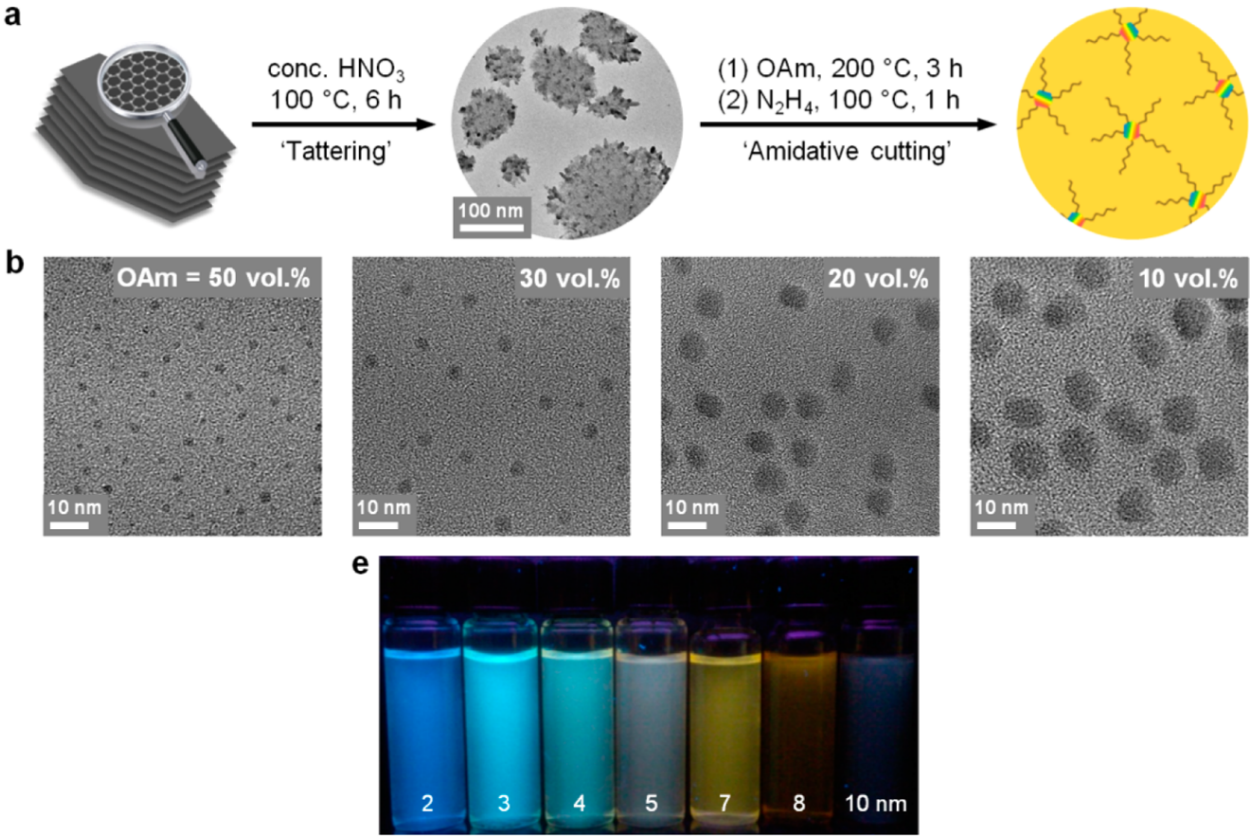

Figure 1. (a) Schematic of tattering graphite, amidative cutting of tattered graphite, and hydrazine treatment to reduce excess oxygenic carbons such as epoxide. (b) TEM images of the GQDs with varied sizes of 2, 4, 7, and 10 nm (left-to-right). The text insets represent the concentration of oleylamine (OAm) in octadecene. (e) Photo of a series of the GQDs with various sizes under a 365 nm UV lamp. The captions represent the size of the GQDs.

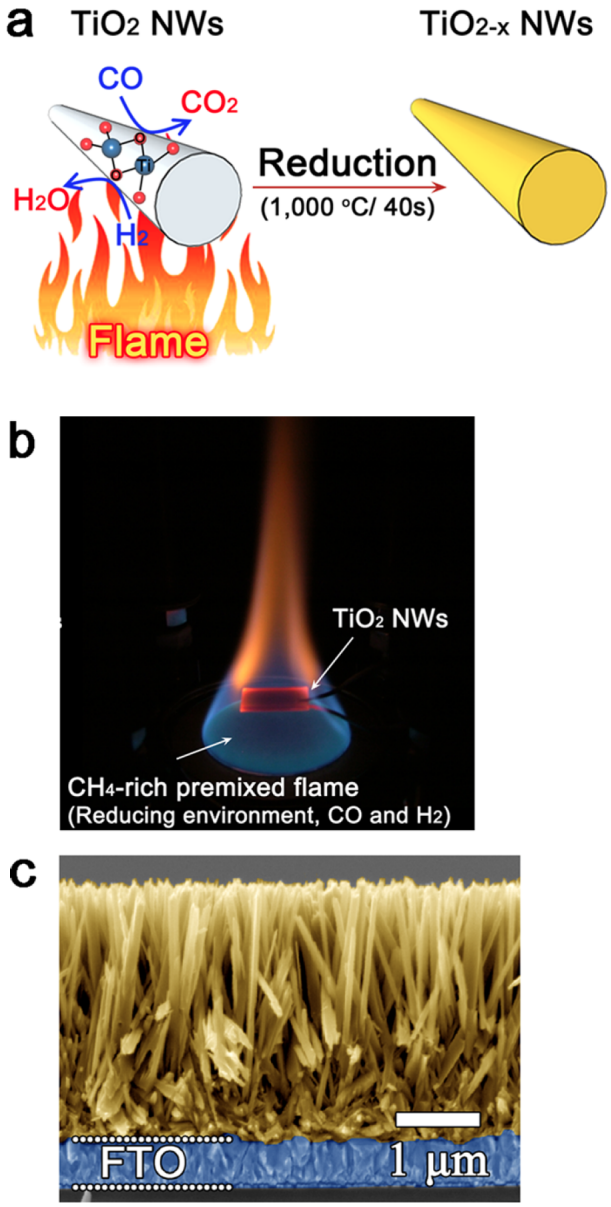

Figure 1. TiO_2 NWs are grown on glass substrates by the hydrothermal method and then annealed in a flame for 5-120s. (a) Schematic illustration of the flame reduction method. (b) A photograph of the flame reduction process. (c) A representative cross-sectional SEM image of the flame-reduced TiO_2 NWs.

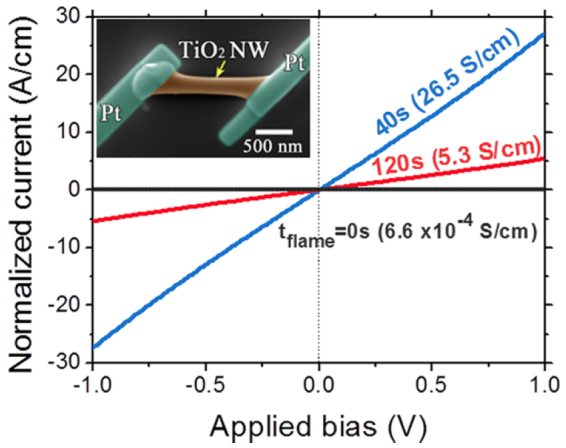

Figure 4. Current−potential curves of single TiO_2 NWs measured in the dark. The inset shows an SEM image of a single TiO_2 NW with metal (Pt) contacts at both ends used for such measurement.

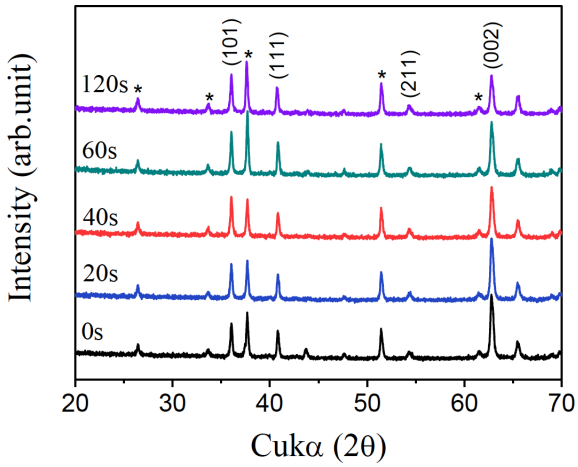

Figure S2. Representative XRD patterns of flame reduced TiO_2 NWs samples. The flame-reduced TiO_2 NWs samples show comparable FWHM values with the untreated sample.

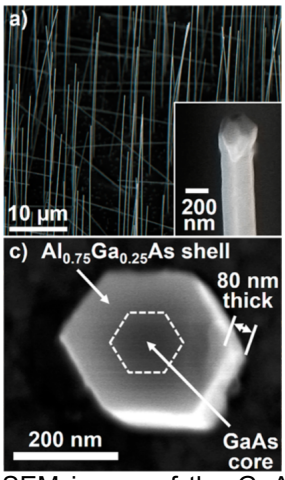

Figure 2. (a) SEM image of the GaAs/AlGaAs core−shell nanowire forest grown on a silicon wafer using droplets of Ga as catalyst precursors. (c) SEM high-resolution image of a nanowire section 80 nm tall.

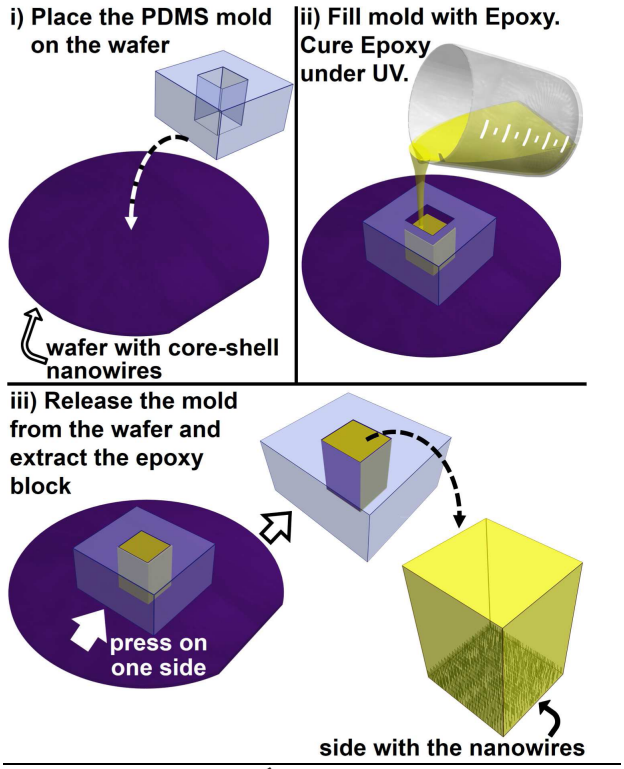

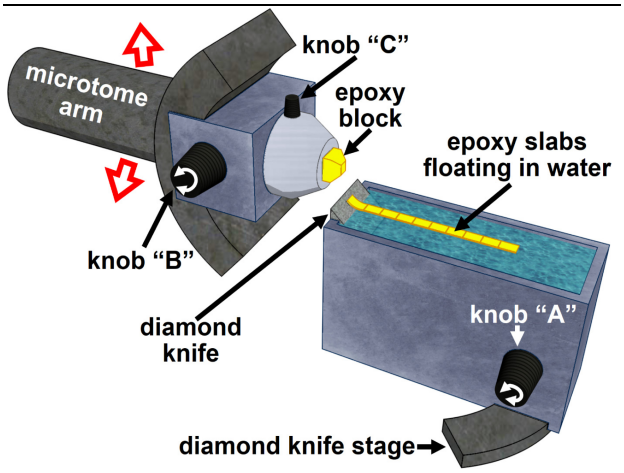

Figures S2 and S5. A PDMS mold approximately 1 cm tall is used to embed the nanowires in epoxy. An ultramicrotome is used to perform nanoskiving.

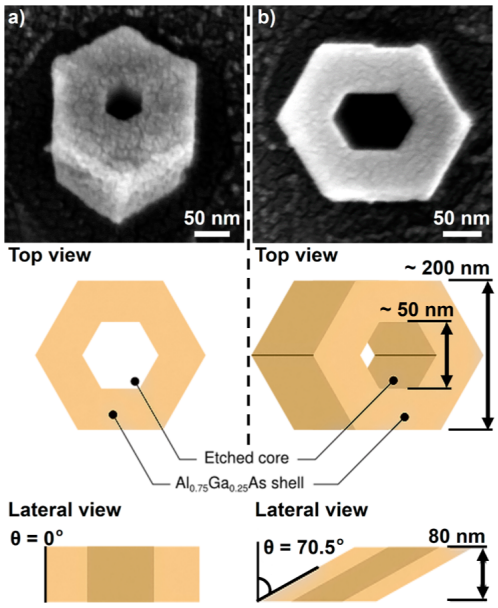

Figure 3. Control of the geometry of the sectioning, and selective etching of the GaAs core of the sectioned GaAs/AlGaAs core−shell nanowires. (a) Scanning electron image of an 80 nm thick slice of a GaAs/AlGaAs nanowire sectioned along its (111) plane after the removal of the GaAs core by citric acid and hydrogen peroxide. (b) Scanning electron image of a slice of a different GaAs/AlGaAs nanowire (also 80 nm thick) sectioned along its (110) plane after the selective etching of the GaAs core. SEM images were taken perpendicular to the plane of the substrate. Schemes representing the top and lateral views of the nanostructures illustrate their dimensions. After cutting a first slab, all the subsequent slabs will contain nanowires with both ends parallel and an inclination angle defined by the cutting angle.

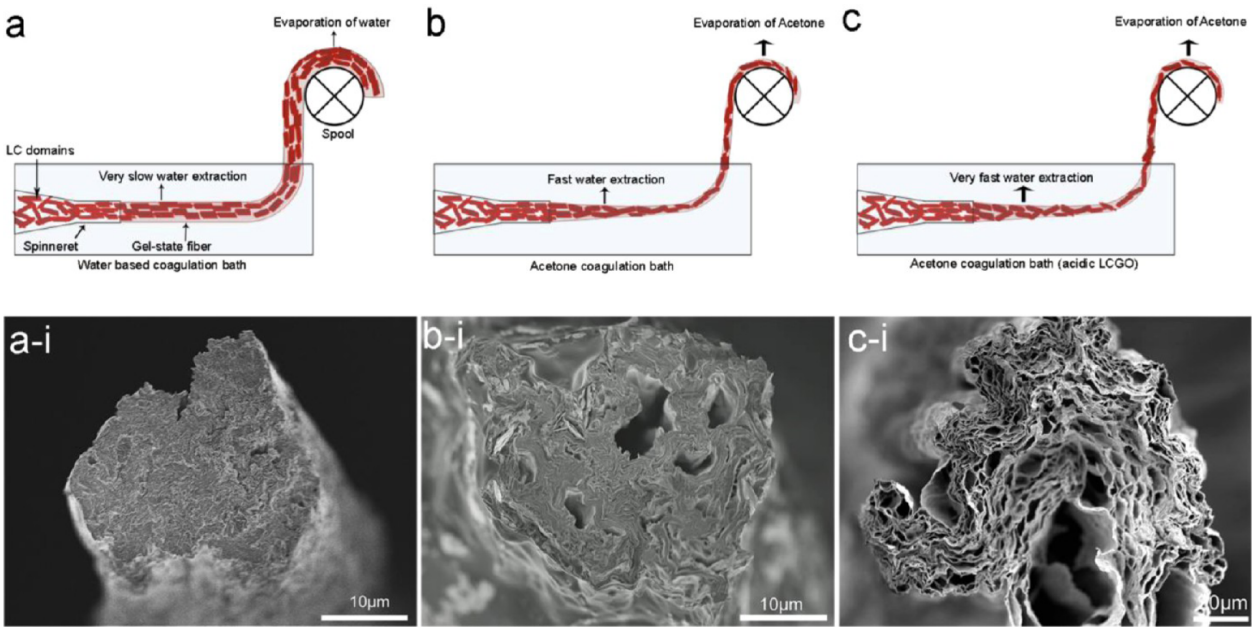

Figure 2. As the graphene oxide liquid crystal dispersion is injected, GO filaments are coagulated instantly. Different coagulation baths produce (a) highly dense to (c) highly porous architectures. (a) Employing a water-based coagulation bath results in slow expulsion of water from the as-injected gel-state fiber-like structure. The fiber can then be taken from the bath and transferred on a spool for the evaporation of the water from the fiber, resulting in a highly dense structure (a-i). (b) Using an acetone coagulation bath results in the high rate of water extraction from the surface as a result of the difference in imbibition rate, consequently leading to higher rate of solidification and porous fiber structure (b-i). (c) Slight acidity (pH ~3) further changes the difference in imbibition rate, resulting in much higher water extraction rate and consequently more porous geometry (c-i).

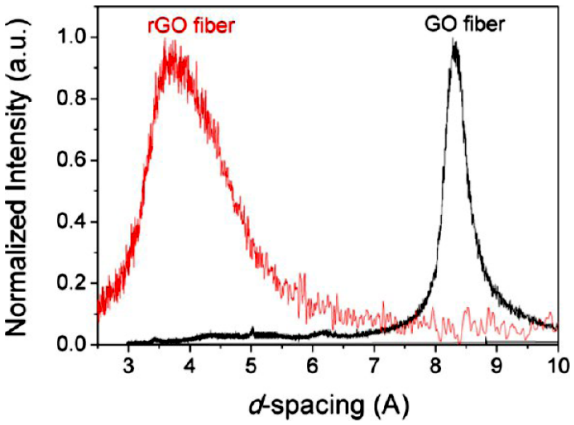

Figure 3. Heat-treatment under vacuum of the graphene oxide fibers at 200-220°C reduces the GO sheets (rGO) as seen in the XRD patterns. For comparison, the *d*-spacing for graphite is 3.35 Å.

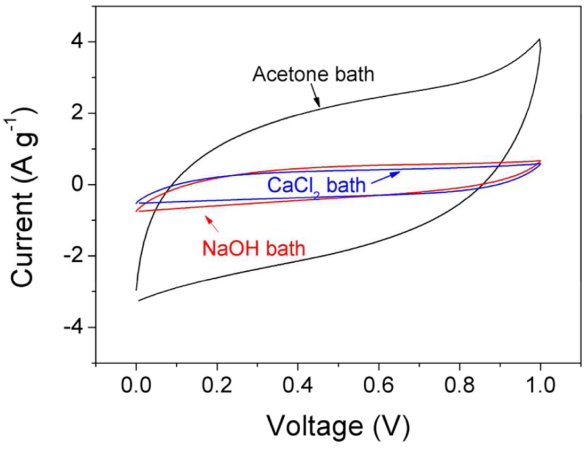

Figure S6. Cyclic voltammograms of graphene fiber yarns produced in acetone bath, alkaline bath (NaOH), and ionic crosslinking using divalent cations bath ($CaCl_2$) in 1M H_2SO_4 at 10 mV s^{-1} clearly showing the superior performance of the fibers produced in acetone bath.

Chem 150 **First Test** February 27, 2013

Interpret the figures by expanding on what is being illustrated, explaining procedures or techniques, indicating why it might be important or making connections to our class readings and laboratory work. Tell more than rewriting the caption. Try to use your interpretation to demonstrate additional knowledge beyond what is shown here. ***All the figures on a given page are from the same paper.***

ACS Nano,, **2013**, *7* (1), pp 818–824 **DOI**: 10.1021/nn305372n, Publication Date (Web): December 12, 2012

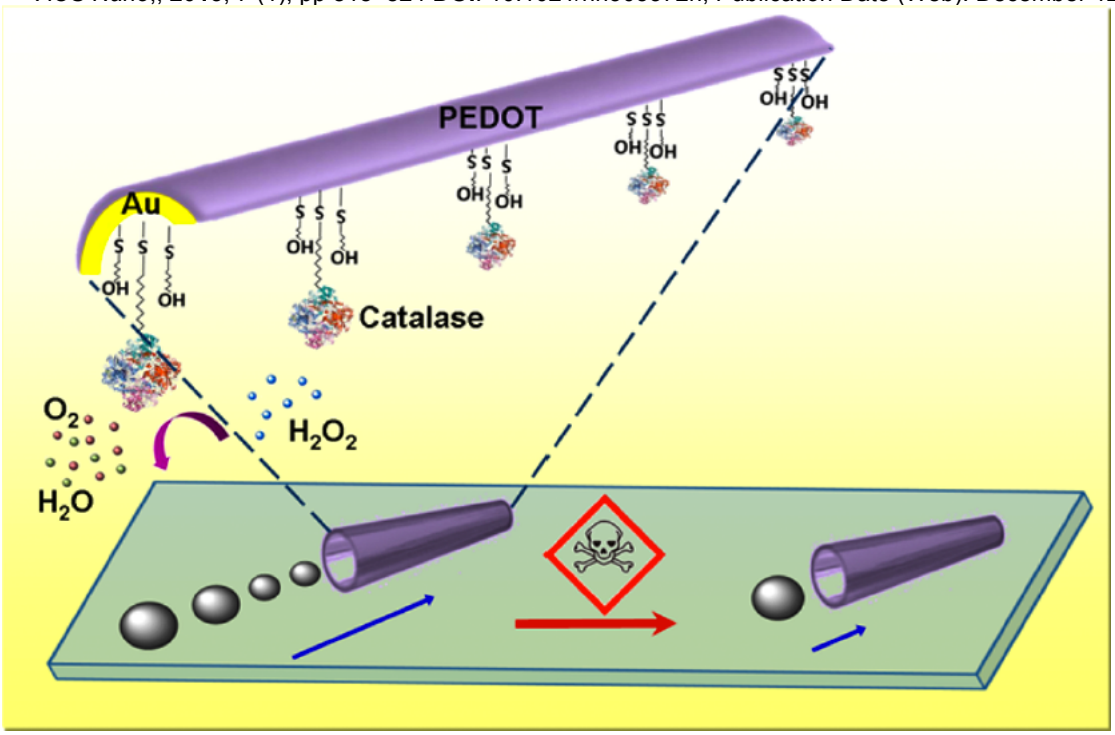

Figure 1. Scheme illustrating the pollutant effect on the microfish locomotion speed through inhibition of the catalase biocatalytic layer (bottom) along with the protocol used for immobilizing the enzyme at the inner gold surface of the tubular microengine through a self-assembled monolayer (top).

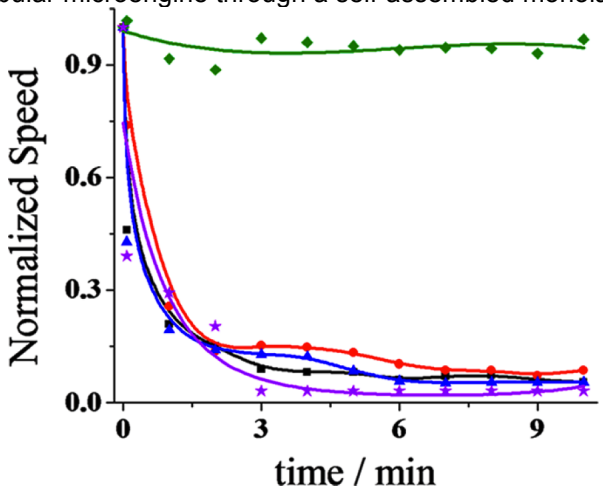

Figure 3. Changes in the swimming behavior of the artificial microfish as a function of time upon exposure to 100 μM Hg (square), 0.6 mM Cu (stars), 25 μM sodium azide (circle), 625 mM aminotriazole (triangle), and a control experiment without the toxins (diamond). Curves were plotted by tracking the normalized microfish speed after exposure to the pollutants.

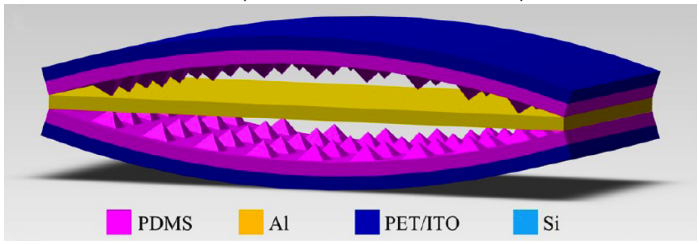

Figure 1a. Schematic view of structural design of the sandwich-shape nanogenerator.

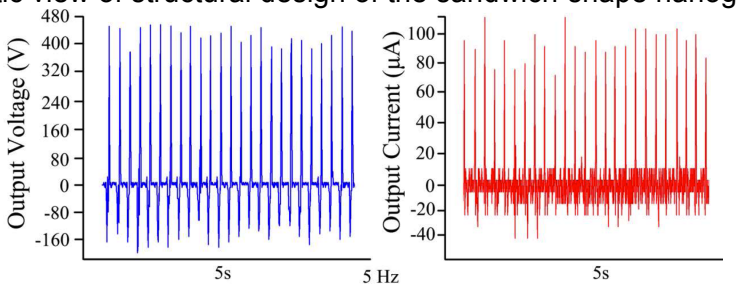

Figure S3. The measured voltage and current of micro/nano dual-scale pyramids under the external force with the frequency of 5 Hz.

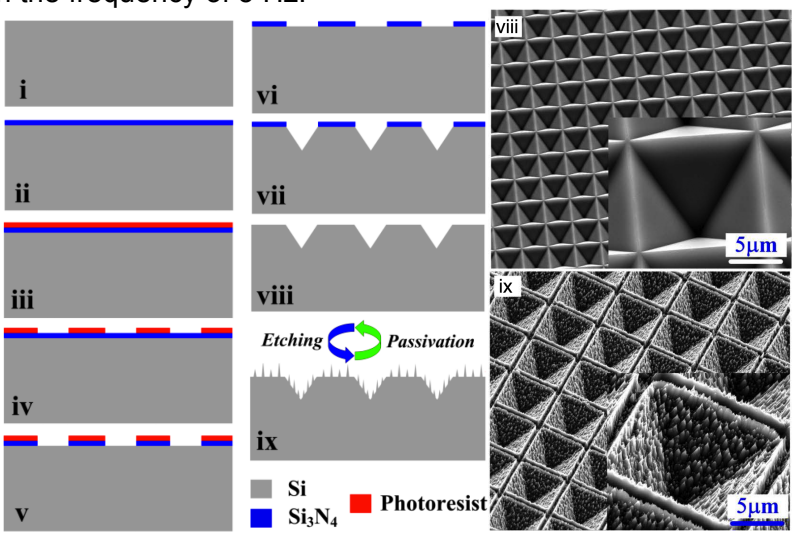

Figure S1. *Left* i) Preparation of 4-inch (100) polished Si wafer; ii) Growth of 1000 Å Si_3N_4 by CVD; iii-iv) Photolithography; v) Pattern transfer to Si_3N_4 by reactive ion etching (RIE) process; vi) Removal of photoresist; vii) KOH (30%, 85°C) wet etching; viii) Removal of Si_3N_4 by RIE; ix) Fabrication of high-dense nanostructures atop microstructures by RIE. *Right* SEM images of micro inverted pyramids and micro/nano dual-scale inverted pyramids.

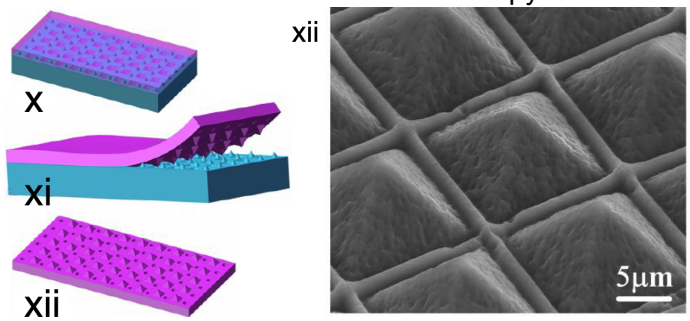

Figure 1b. *Left* x-xii) Fabrication of PDMS film with micro/nano dual-scale structures replicated from silicon mold. *Right* SEM image of the 40°-tilted view of the PDMS surface.

Nano Lett., **2013**, *13* (2), pp 581–585 **DOI:** 10.1021/nl304111v, Publication Date (Web): January 29, 2013

Preparation of radioactive ^{198}Au-doped AuNCs. Radioactive ^{198}Au-doped AuNCs were prepared via the galvanic replacement reaction between Ag nanocubes and an aqueous solution containing $H^{198}AuCl_4$. To the aqueous suspension of Ag nanocubes (~1 nM), we added dropwise (30 mL h^{-1}) a mixture of the aqueous solution containing $H^{198}AuCl_4$ (0.32 to 70 μCi/mL) and conventional $HAuCl_4$ (0.75 mM). Aliquots were taken from the solution and analyzed by UV-vis spectrophotometry to monitor the formation of AuNCs (it took approximately 1 h). The solution was purified by centrifugation at 12,000 rpm for 8 min and washed five times with ultrapure water to obtain ^{198}Au-doped AuNCs. The yield of radiolabeling was about 80%, as determined using gamma counting.

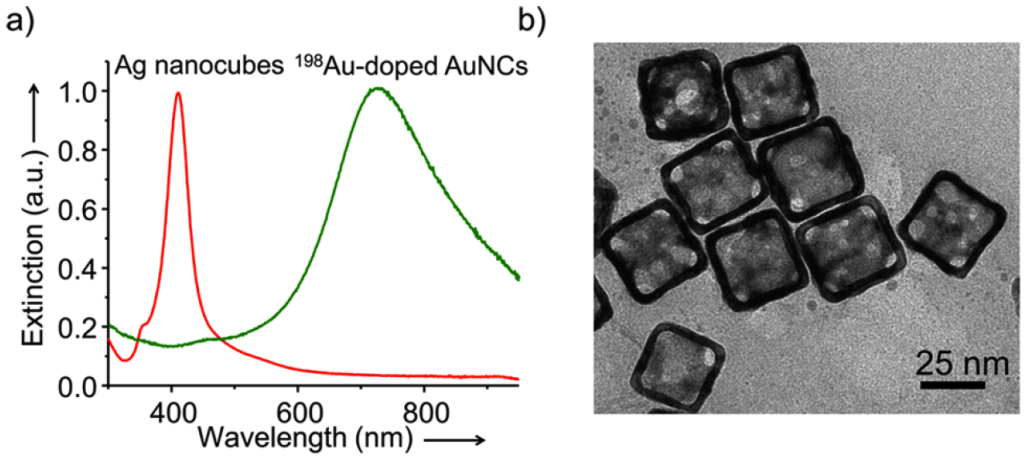

Figure 1. (a) Normalized UV−vis spectra taken from aqueous suspensions of the Ag nanocubes and ^{198}Au-doped AuNCs (after the isotope had decayed for one month), respectively. (b) TEM image of the ^{198}Au doped AuNCs. The image was recorded after the ^{198}Au had decayed for one month.

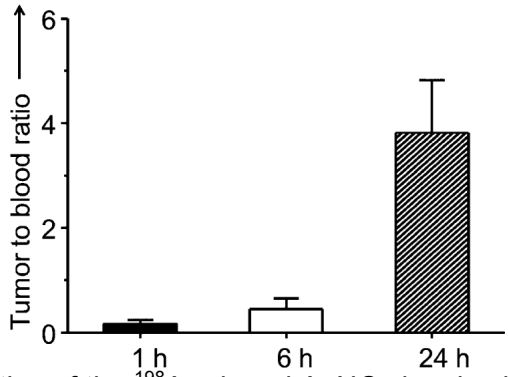

Figure 3. Tumor-to-blood ratios of the ^{198}Au-doped AuNCs in mice bearing EMT-6 tumors at different times post tail vein injection.

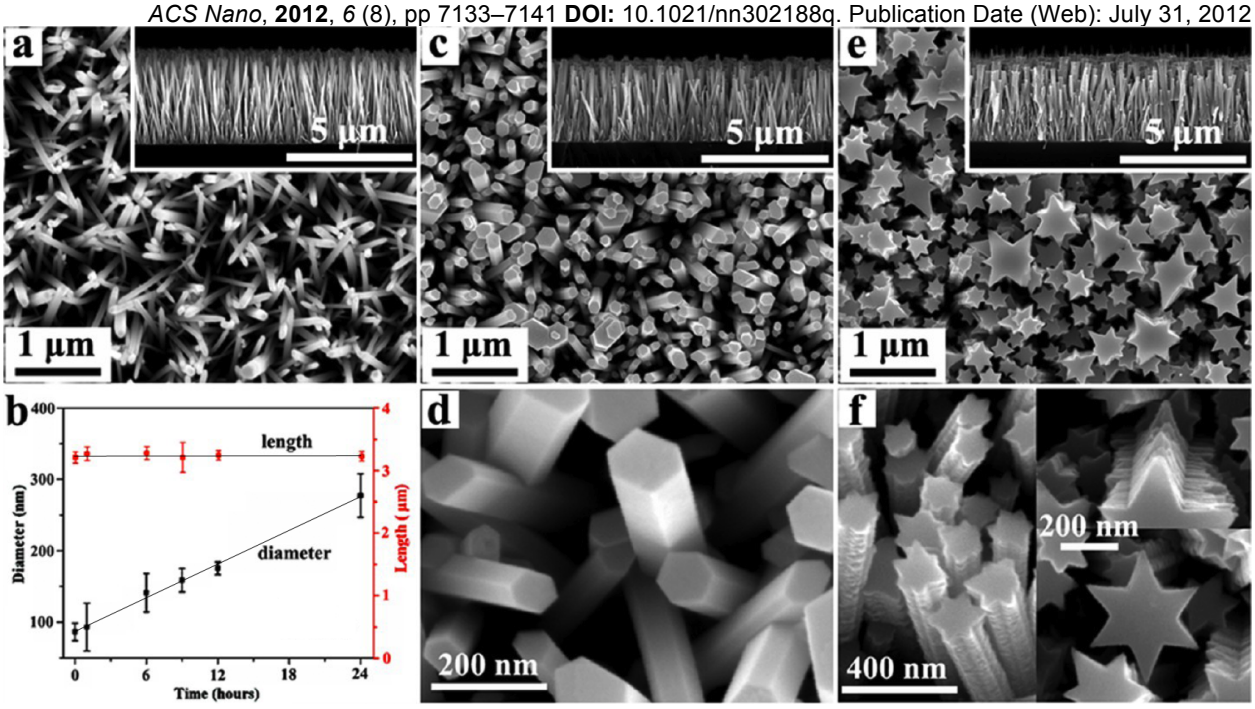

Figure 4. (a) SEM image of ZnO nanowires used as the seeds. (b) Plots of the average length and diameter of ZnO nanowires as a function of the growth time by the PEG-assisted secondary growth (1 mL of PEG). Morphologies of two important stages: 6 h (c, d) and 24 h (e, f).

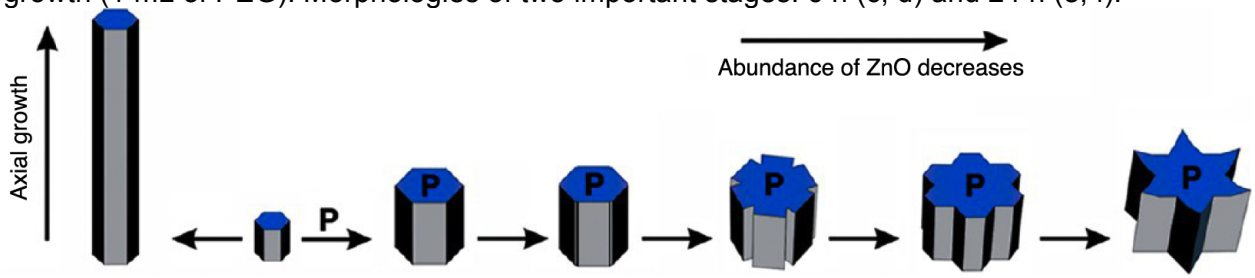

Figure 2. Pictorial representation of the mechanism for the formation of single-crystalline ZnO hexabranched nanostructures. PEG is represented as P in the scheme.

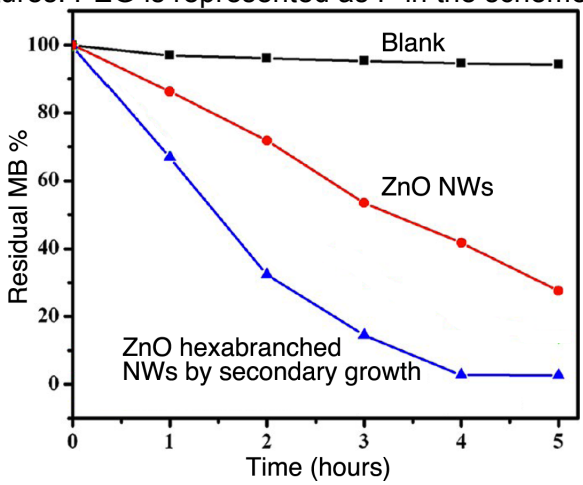

Figure 6. Degradation of methylene blue organic dye (4 mL, 2μM) photocatalyzed by normal ZnO nanowires (2 cm^2), and secondarily grown ZnO hexabranched nanowires (2 cm^2). All three solutions were exposed to a UV lamp with a wavelength of 254 nm and a power of 15 W.

Chem 150 **First Test** February 29, 2012

Interpret the figures by expanding on what is being illustrated, explaining procedures or techniques, indicating why it might be important or making connections to our class readings and laboratory work. Tell more than rewriting the caption. Try to use your interpretation to demonstrate additional knowledge beyond what is shown here.
All the figures on a given page are from the same paper.

ACS Nano, **DOI:** 10.1021/nn203979n, Publication Date (Web): January 21, 2012

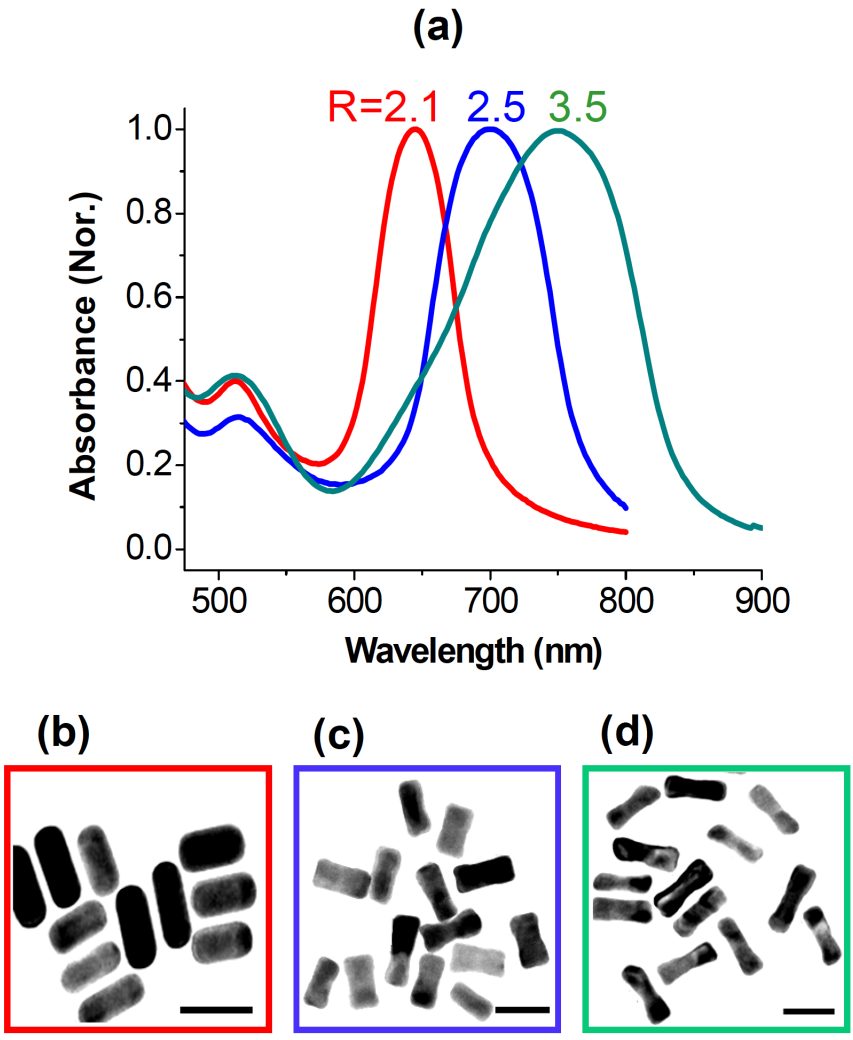

Figure 1. (a) Absorption spectra of AuNRs taken in aqueous solutions with average aspect ratios of 2.1 (left), 2.5 (middle) and 3.5 (right). (b-d) Corresponding representative TEM images of AuNRs. The scale bar dimension is 50 nm.

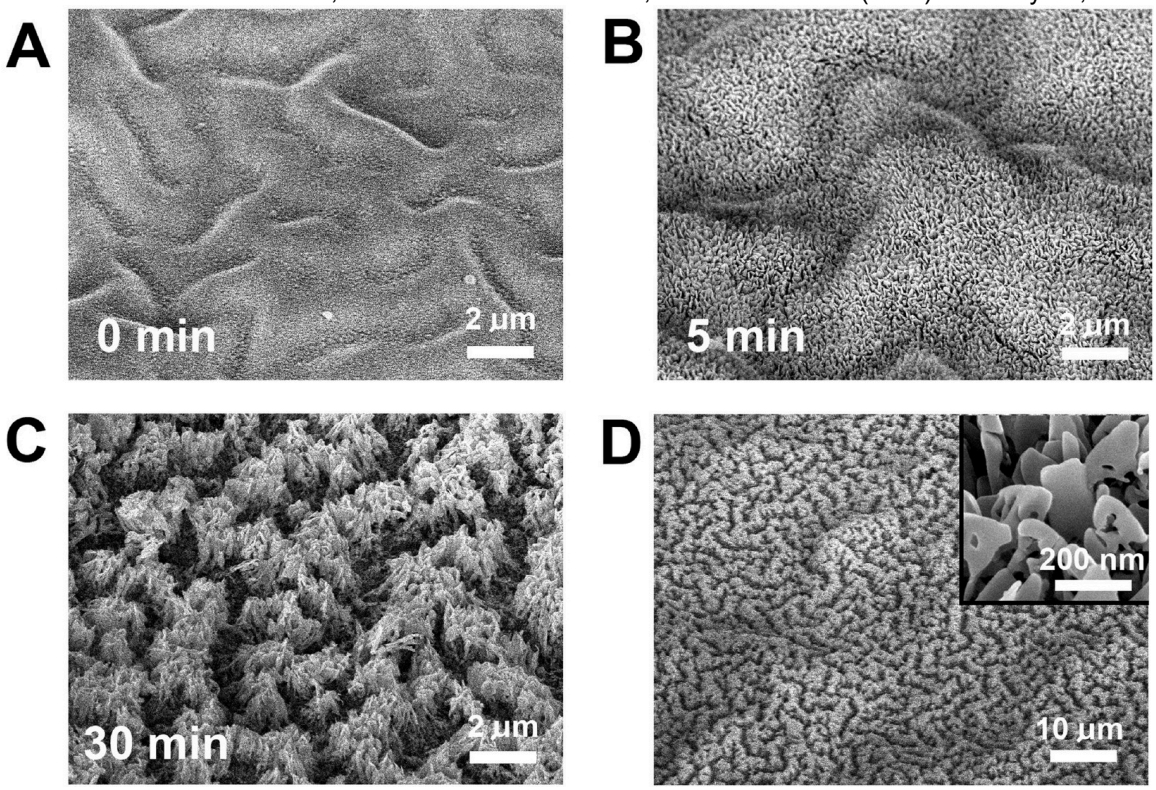

Figure 6. Hierarchical nanoflake structure of Ag and its superhydrophobic surface characteristic. (A-C) SEM images of the evolution of surface texture with varying plasma-ashing time. An initial wrinkled surface (A, 0 min) is roughened with nanoscale Ag flakes (B, 5 min), and further developed to hierarchical nanoflake wrinkles (C, 30 min). (D) Low-magnification SEM image for C. Intrinsically formed microscale wrinkles are clearly manifested. The inset shows a highly magnified image of the vertical Ag nanoflake structure.

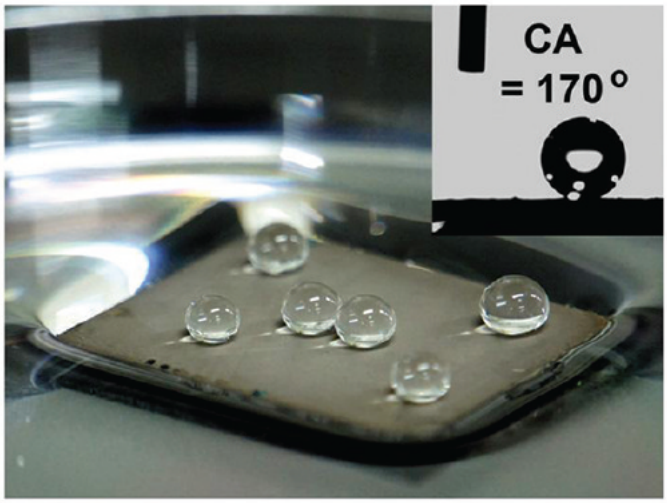

Figure 7. Superhydrophobic property of the surface of the hierarchical nanoflake structure.

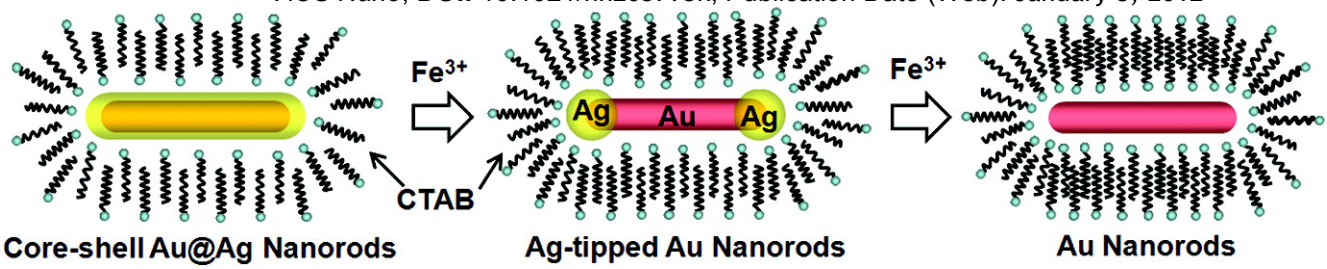

Scheme 1. Illustration on the possible etching mode of Au@Ag core-shell nanorods induced by $FeCl_3$.

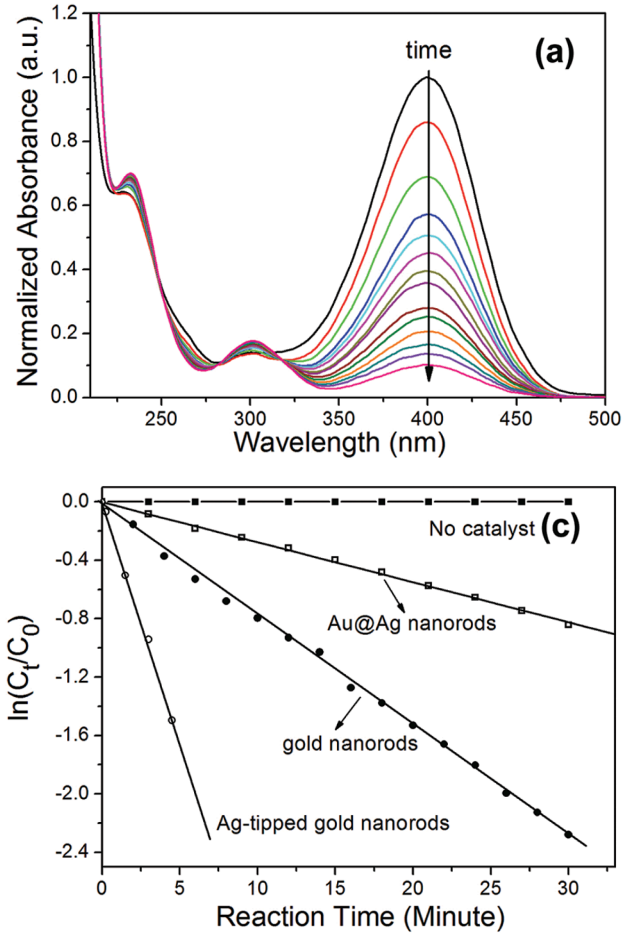

Figure 6. (a) Evolution of the UV-vis absorption spectra of *p*-nitrophenol reduced by $NaBH_4$ in the presence of gold nanorods. (c) Plots of $\ln(C_t/C_0)$ versus reaction time for different nanorods as the catalyst.

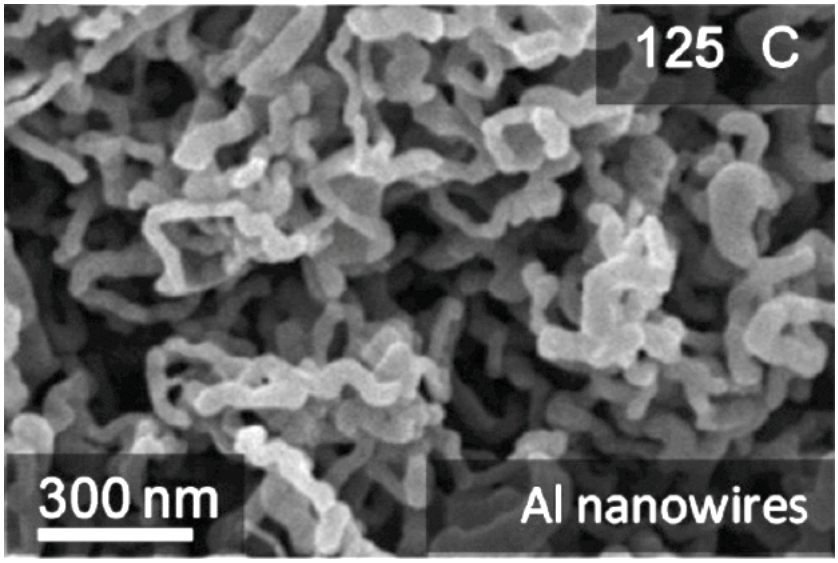

Figure 2. SEM micrograph of CVD deposition of Al NWs onto rough Cu foils at 125 °C.

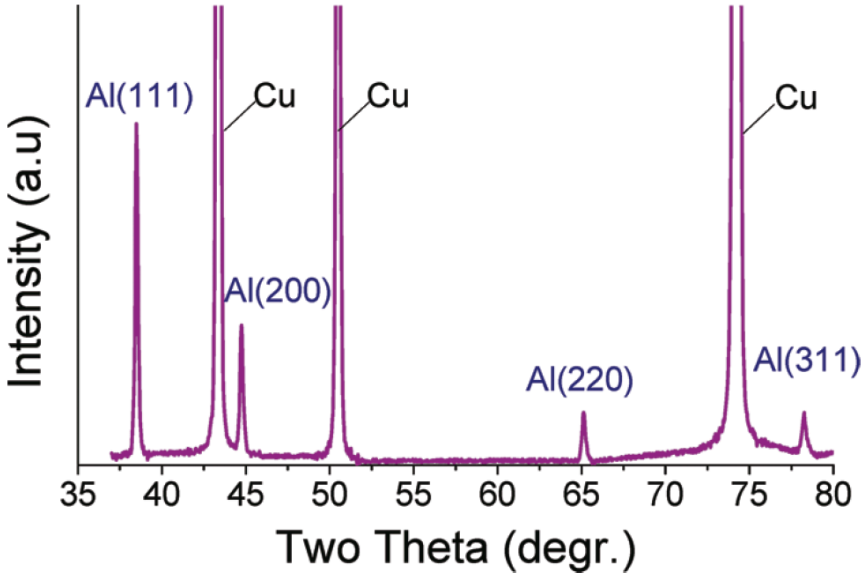

Figure 6. XRD pattern of Al nanowires grown on a rough Cu foil at 125 °C.

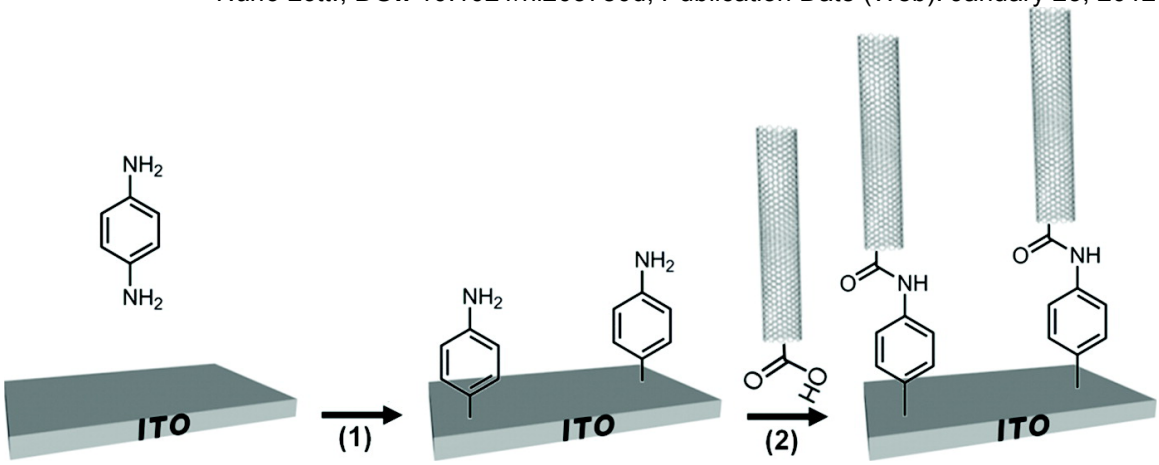

Figure 1. Diagrammatic representation of (1) the electrochemical grafting of an arylamine to the ITO surface and (2) its coupling to SWCNTs yielding vertically-aligned SWCNTs on a ITO surface.

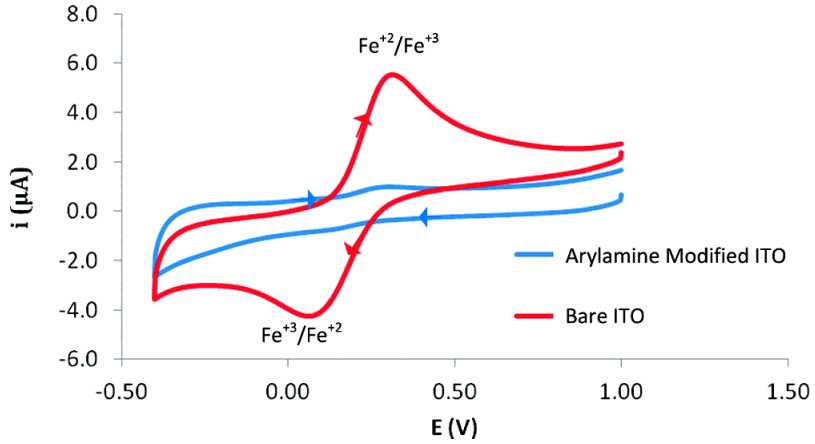

Figure 2. Typical cyclic voltammograms obtained for solutions of 250 μM ferricyanide with 50 mM phosphate buffered pH 7 saline at unmodified and at arylamine-modified electrodes.

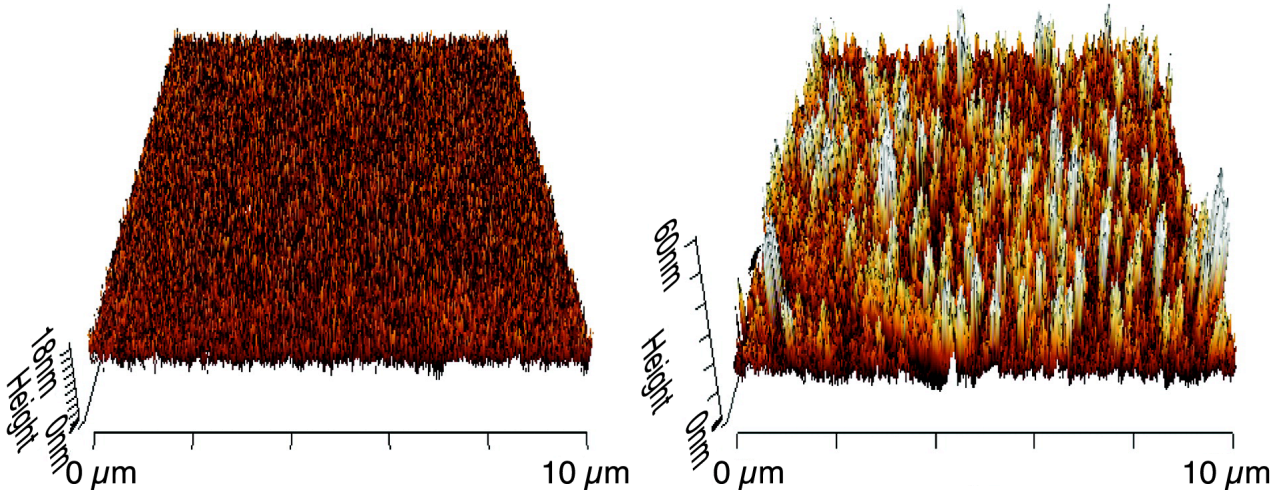

Figure 4. Typical AFM images of arylamine modified ITO (left), and SWCNT modified ITO (right).

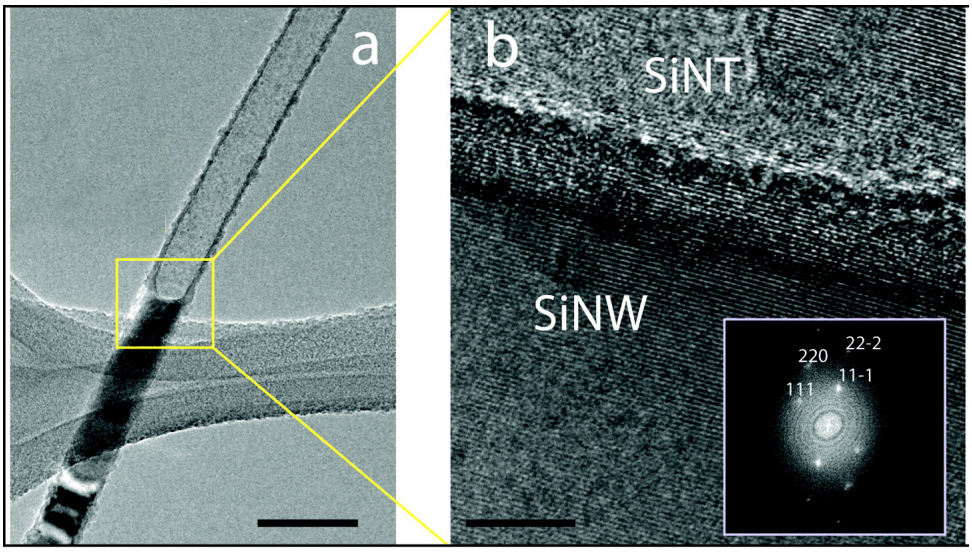

Figure 5. SiNW-SiNT heterostructure. (a) Low-resolution TEM image of a typical straight wire−tube hybrid structure. Scale bar is 85 nm. (b) High-resolution TEM image of the junction between the SiNW and the SiNT showing a single crystalline structure and relatively abrupt interface. Scale bar is 5 nm.

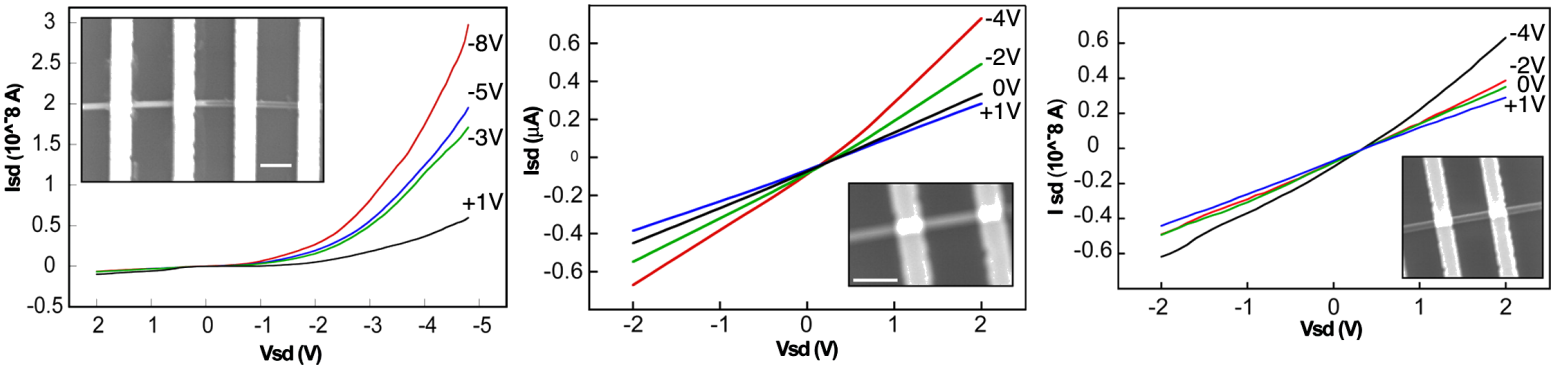

Figure 6. SiNT-SiNW-based device. (left) *I*−*V* characteristics ($V_{NT□NW}$) of p-type SiNT-NW isotype homojunction device measured for different V_{gs} gate bias voltages. Inset: scanning electron microscopy image of the device structure. Scale bar is 446 nm. (middle) *I*−*V* data recorded from the wire portion at indicated gate voltages. Inset: scanning electron microscopy image of the wire portion device structure. Scale bar is 444 nm. (right) *I*−*V* data recorded from the tube portion at indicated gate voltages. Scanning electron microscopy image of the tube portion device structure. Scale bar is 600 nm.

Chem 150 **First Test** March 2, 2011

Interpret the figures by expanding on what is being illustrated, explaining procedures or techniques, indicating why it might be important or making connections to our class readings and laboratory work. Tell more than rewriting the caption. Try to use your interpretation to demonstrate additional knowledge beyond what is shown here.
All the figures on a given page are from the same paper.

Nano Lett., **2011**, *11* (2), pp 786-790

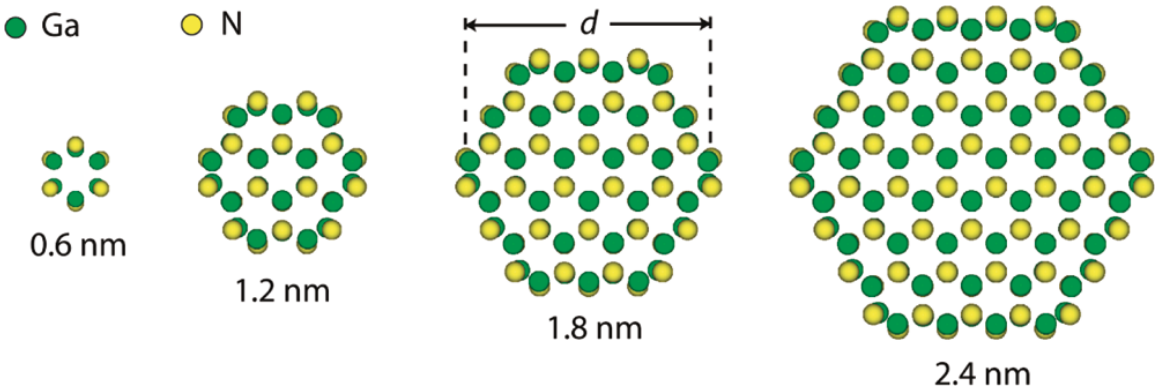

Figure 1. Cross sections of modeled GaN nanowires.

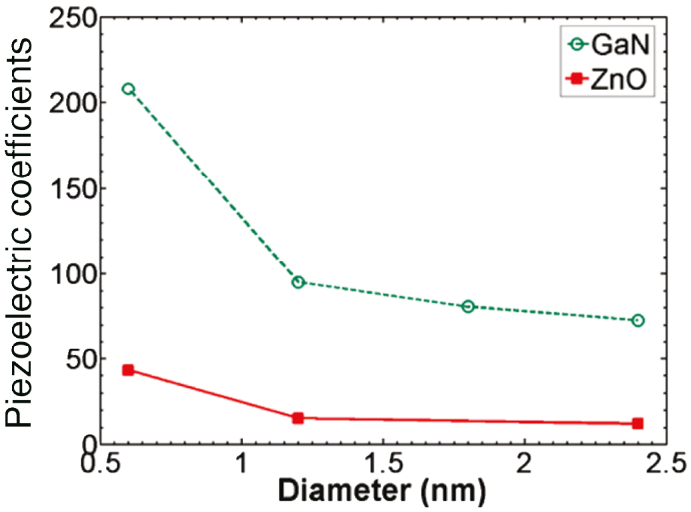

Figure 2. Calculated piezoelectric coefficients of GaN and ZnO nanowires compared to their respective bulk values.

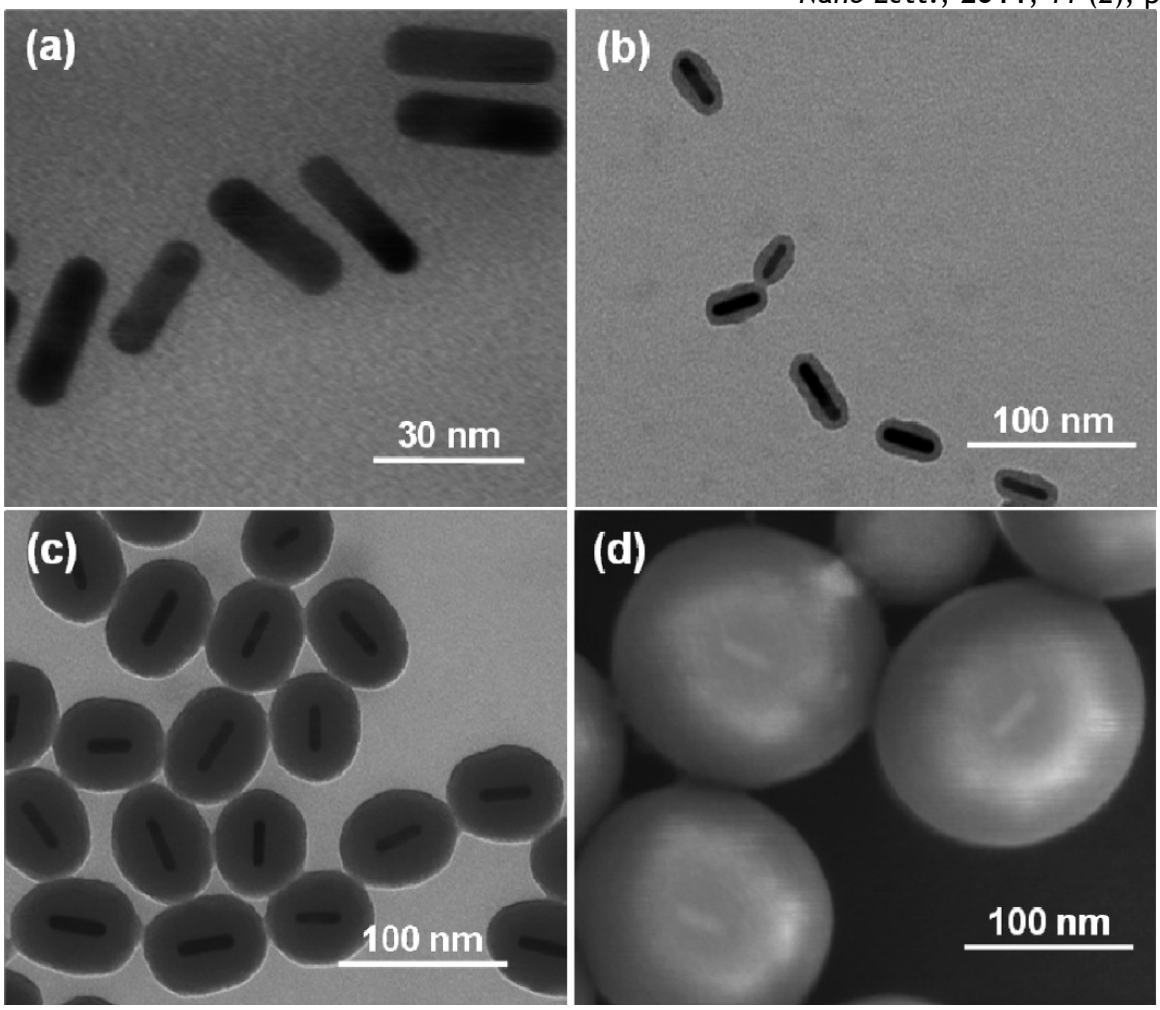

Figure 1. Cetyltrimethylammonium bromide (CTAB) stabilized gold nanorods were first prepared with the seed-mediated growth method. Then CTAB was replaced by $HS(CH_2CH_2O)_7CH_3$ (mPEG-thiol) through ligand exchange, and then silica was grown onto the PEGylated gold nanorods via the modified Stöber method using tetraethyl orthosilicate (TEOS). (a) TEM image of PEGylated gold nanorods. TEM images of gold-silica core-shell nanorods with (b) 6 ± 0.5 nm (N = 100) and (c) 20 ± 3.6 nm (N = 100) thickness of silica coating. (d) SEM image of gold-silica core-shell nanorods with 75 ± 5.0 nm (N = 100) thickness of silica coating (the silica shell is too thick for TEM).

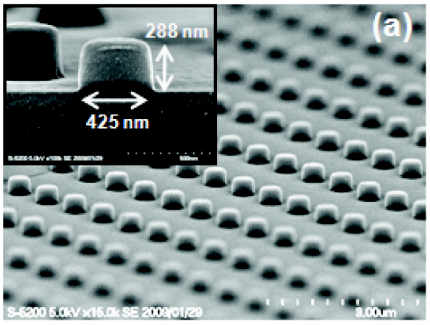

(a) SEM image of nanopillar template

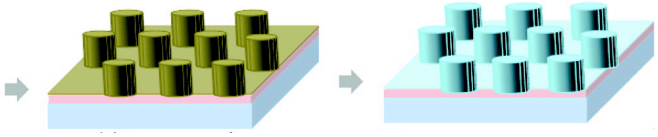

(b) Au sputter

(c) Polymer coating with layer-by-layer (LBL) assembly technique.

The substrate was immersed in an aqueous solution of poly(dimethyldiallylammonium chloride) (PDDA, 1 mg/mL) for 10 s, rinsed with ion-exchanged water for 10 s, and dried with nitrogen gas flow for 30 s.Then the substrate was immersed in an aqueous solution of poly(styrenesulfonate) (PSS, 1 mg/mL) for 10 s, rinsed with ion-exchanged water for 10 s, and dried with nitrogen for 30 s. This process was repeated 50 times to form alternating layers of PDDA and PSS on the NP surface.

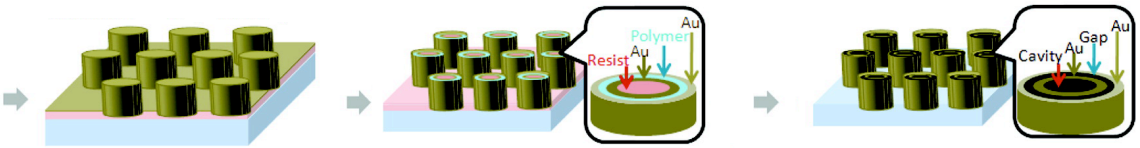

(d) Au sputter

(e) Reactive ion etching to remove top surface

(f) Removal of template and polymer layer

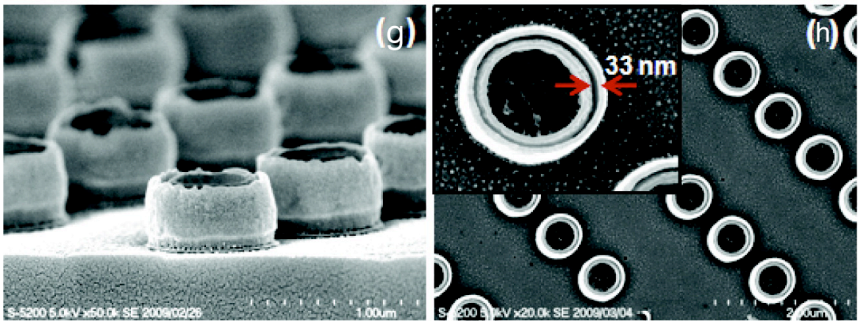

SEM image of (g) Au DNPs with hollowed nanogap after removal of template and polymer layer, and (h); top view of Au DNP arrays with nanogap width of 33 nm.

Figure 1. Fabrication process for Au double nanopillar (DNP) arrays.

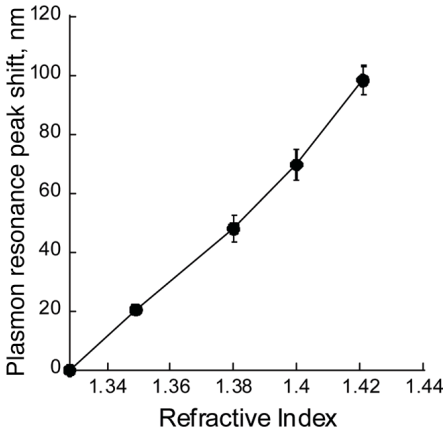

Figure 6. As the refractive index of the solvent filling the 33 nm nanogap increases, the plasmon resonance of the Au DNP array shifts to a longer wavelength. (The ratio of ethylene glycol to deuterium water was changed from 0, 20, 50, 70, and 90% by volume, giving refractive indices of 1.328, 1.349, 1.380, 1.400, and 1.421, respectively.)

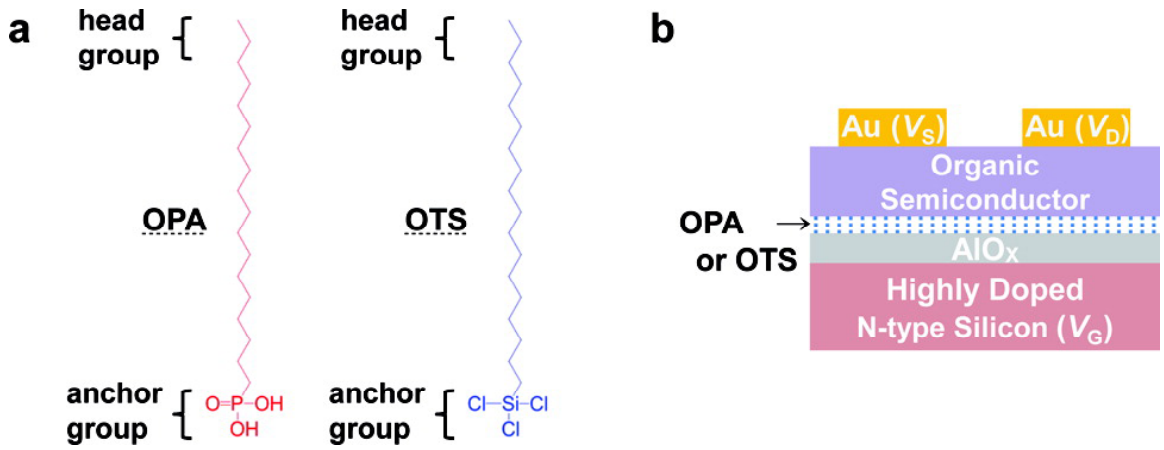

Figure 1. (a) Chemical structures of SAM molecules and (b) a schematic of the OFETs. The OPA and OTS SAMs on aluminum oxide (AlO_X) generated different dipole moments and built-in voltages and successfully adjusted the energy levels of electrons in the channel, which in turn resulted in a significant change in the transistor turn-on voltage.

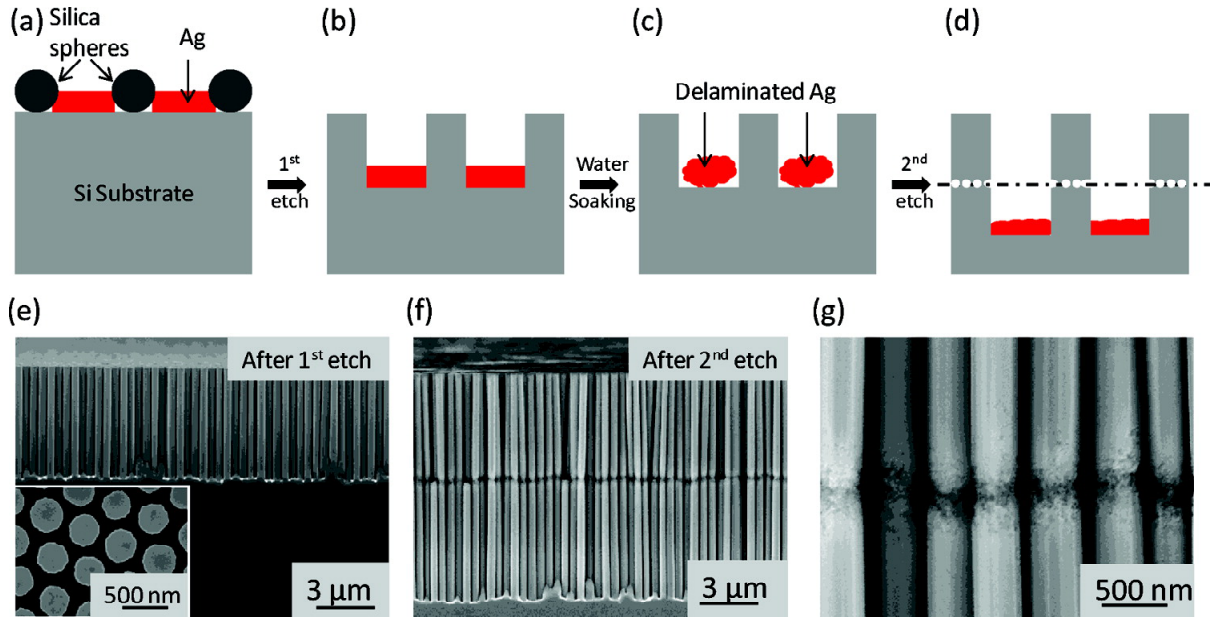

Figure 1. Schematic of the fabrication procedure for a cracked SiNW array. (a) Silica (SiO_2) spheres were synthesized by a modified Stöber synthesis method, deposited as a monolayer on a Si(100) wafer via Langmuir-Blodgett assembly, followed by e-beam evaporation of a 50 nm thick silver film. The SiO_2 spheres were then removed ultrasonically in isopropyl alcohol (IPA), resulting in a honeycomb-pattern silver film. (b) a SiNW array is formed by immersing the Si wafer in an etchant solution of 4.6 M hydrofluoric acid (HF) and 0.4 M hydrogen peroxide (H_2O_2). (c) Ag is delaminated from Si after soaking the wafer in 75 °C DI water for 3 h, (d) a horizontal crack is formed at the start of the second etch, along with the elongation of the SiNWs. SEM images of SiNWs (e) after the first etch, (f) after the second etch, and (g) with a zoom-in view of the crack.

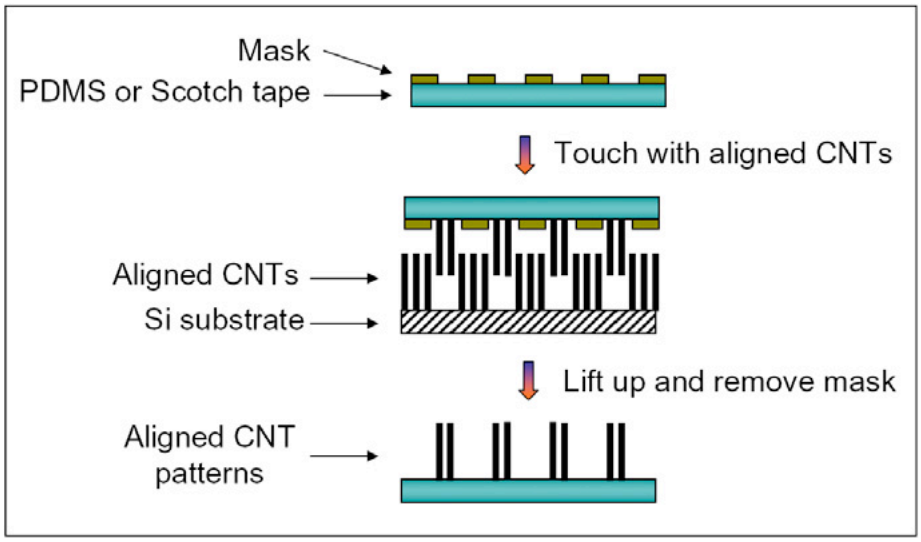

Figure S1. Schematic diagram of the formation of primarily patterned CNTs on PDMS or Scotch tape surface.

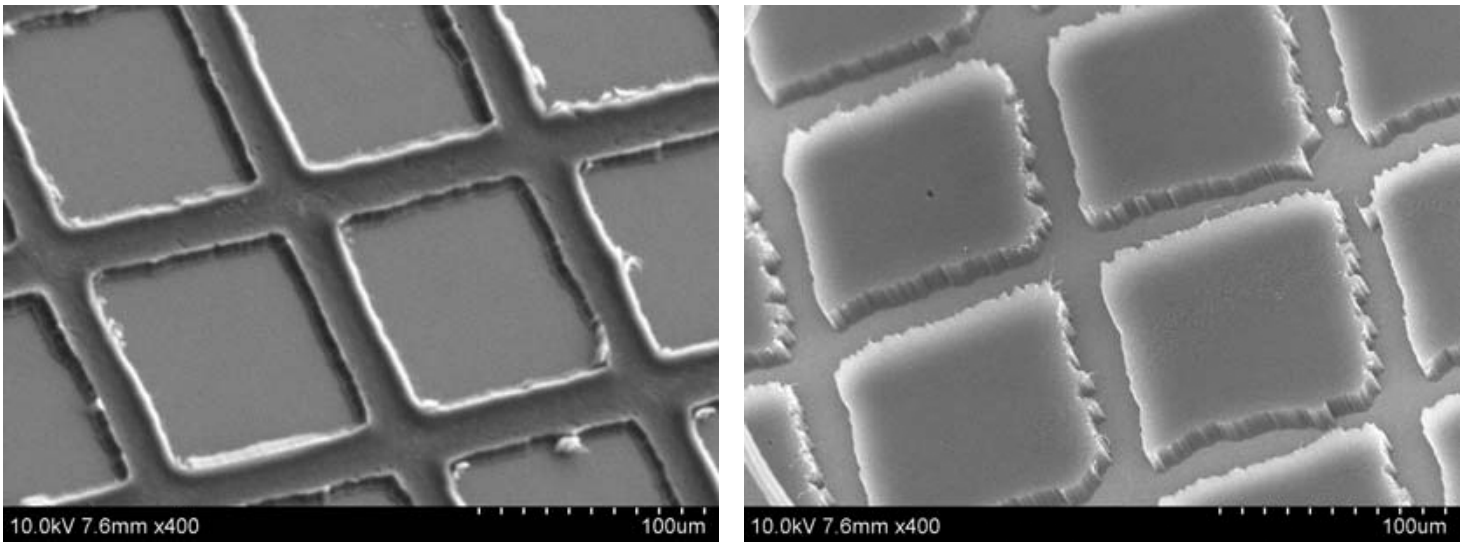

Figure S2. SEM images of the formed patterns on Si wafer and PDMS (also applicable to Scotch tape) of aligned CNTs by first contact transfer (Figure S1).

Interpret these figures by expanding on what is being illustrated, explaining procedures or techniques, indicating why it might be important and making connections to our class readings and laboratory work. Try to use your interpretation to demonstrate what you have learned.

ACS Nano, January 2010, 10.1021/nn901250w

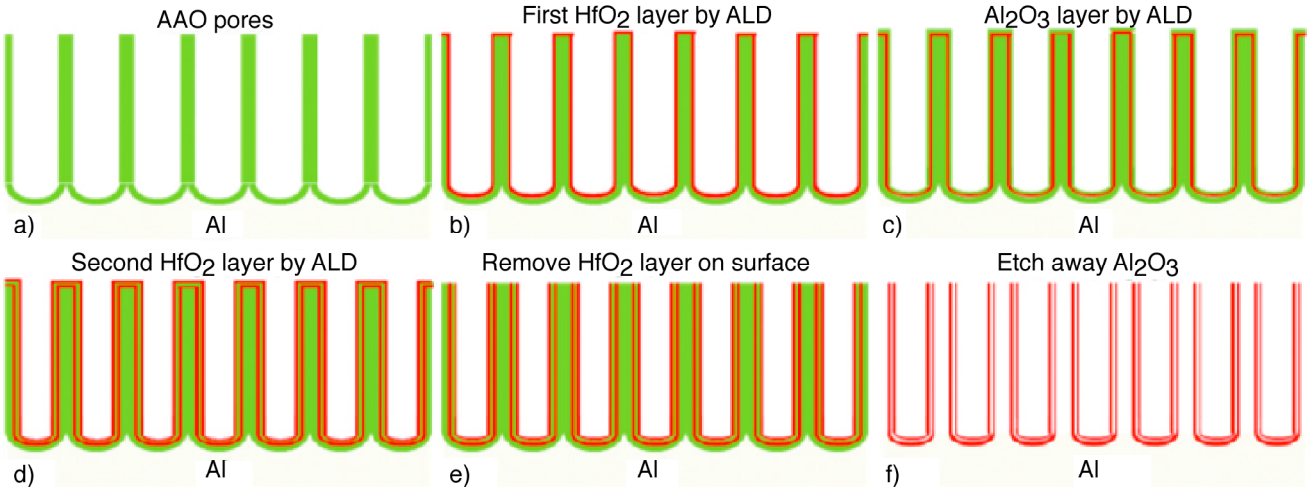

Nested multiple-walled coaxial nanotube structures of transition metal oxides, semiconductors, and metals were successfully synthesized by atomic layer deposition (ALD) techniques utilizing nanoporous anodic aluminum oxide (AAO) as templates.

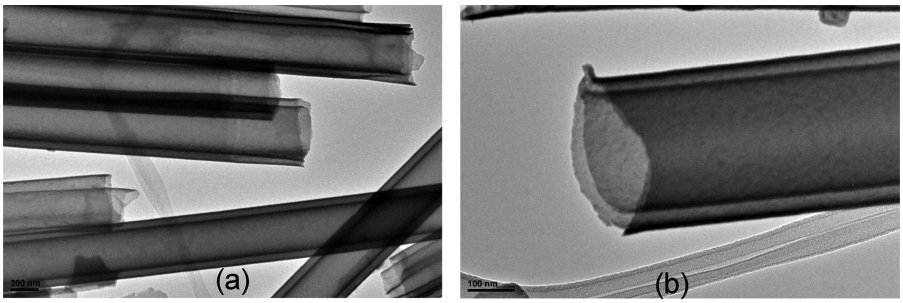

TEM view of resultant coaxial HfO_2 nanotubes following release from the AAO template and removing the sacrificial spacer Al_2O_3 layer

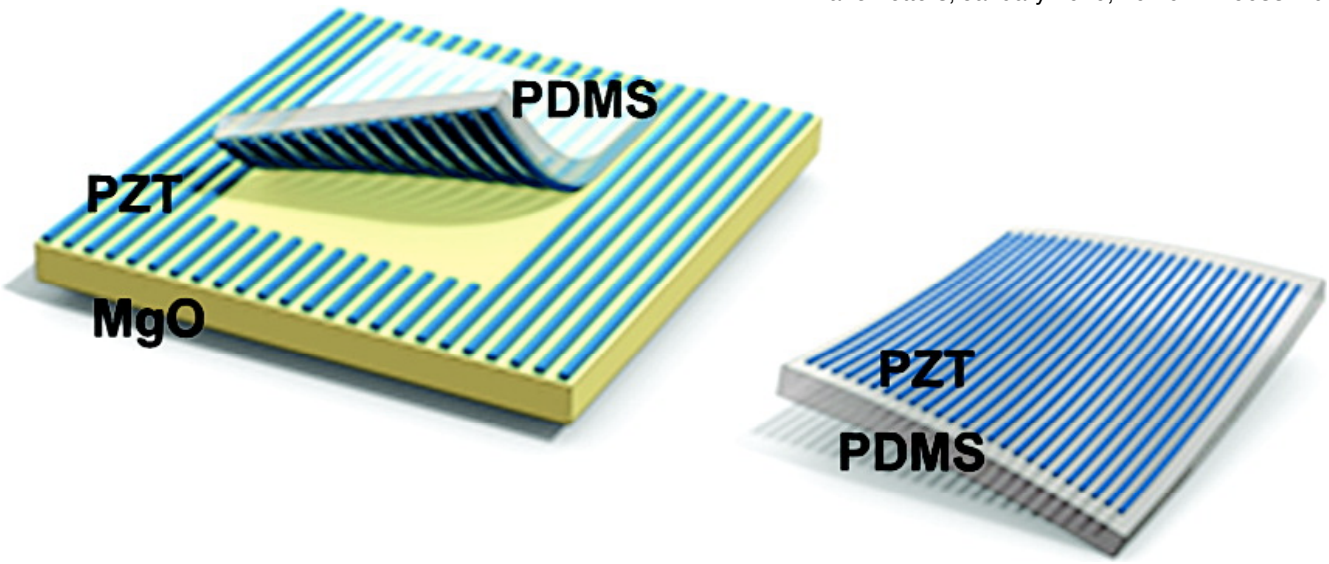

Crystalline lead zirconate titanate (PZT) ribbons are synthesized on an MgO host substrate, which is subsequently etched, and the ribbons are transfer printed onto flexible PDMS rubber.

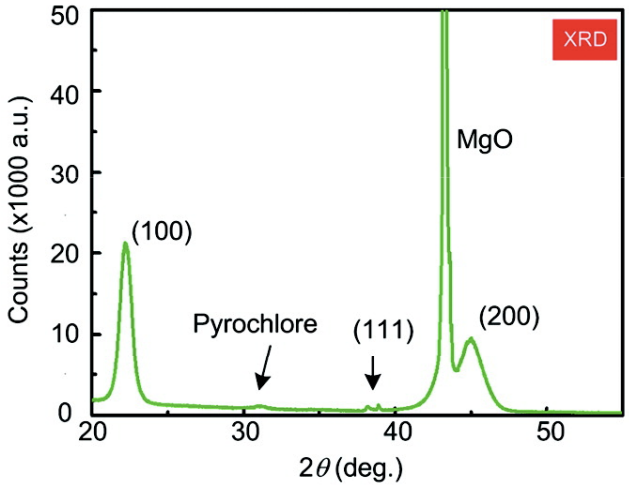

XRD θ-2θ scan of a PZT thin film prepared on MgO and heat-treated at 750 °C.

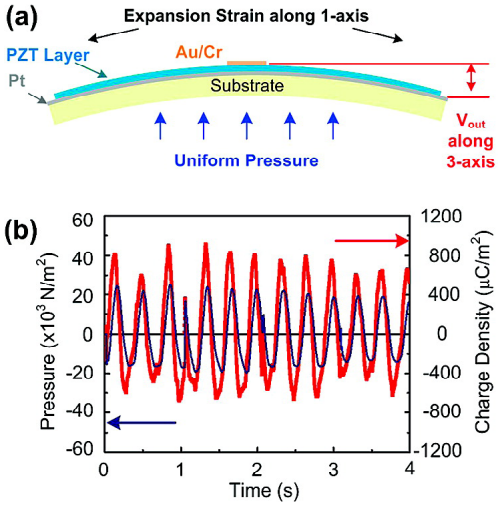

(a) Schematic of a specimen indicating piezoelectric bending and measurement. The PZT layer, top and bottom contact electrodes and substrate are indicated. (b) Oscillating pressure (left axis) and induced dielectric displacement (right axis).

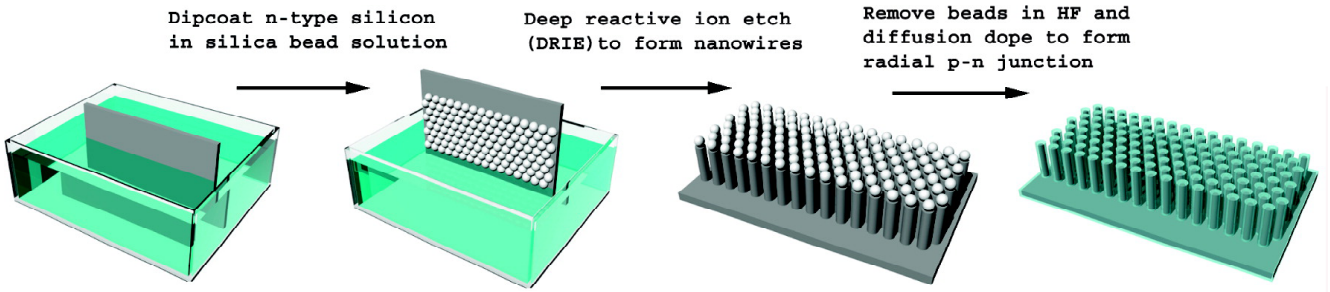

Ordered silicon nanowire array fabrication scheme. The fabrication consisted of three major steps depicted above: dip coating an n-type silicon wafer in an aqueous suspension of silica beads to get a close-packed monolayer; deep reactive ion etching (DRIE) using the beads as an etch mask to form nanowires; bead removal in HF and boron diffusion to form the radial p-n junction.

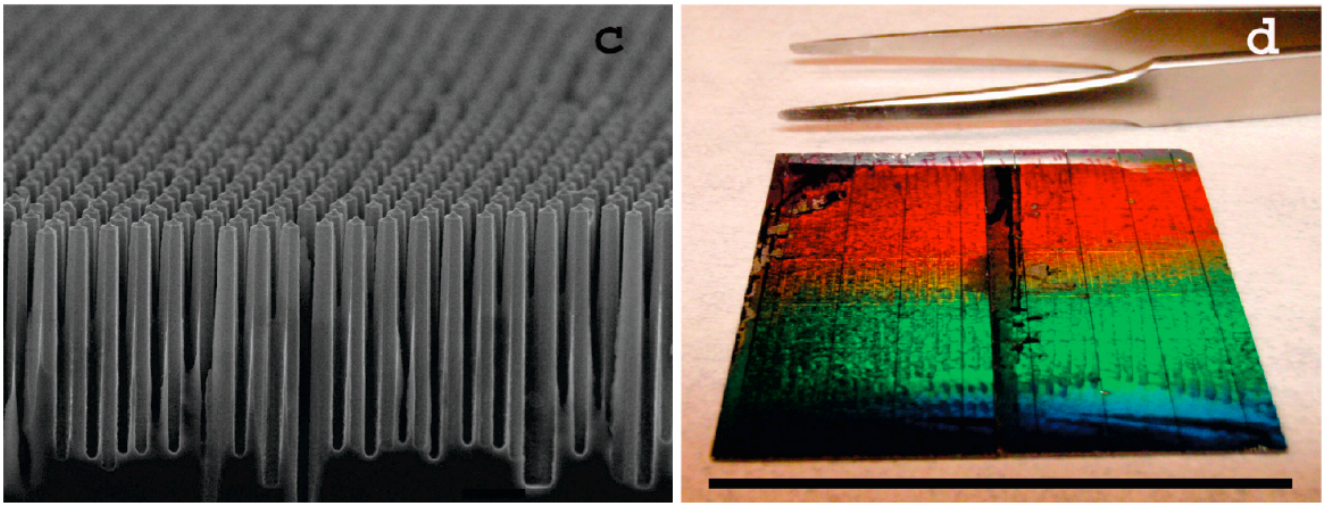

(c) Tilted cross-sectional SEM of the solar cell in panel b. (d) Tilted optical image of silicon nanowire radial p-n junction solar cell arrays. The color dispersion demonstrates the excellent periodicity present over the entire substrate. Scale bar is 4 cm.

Nanoscale, February 2010, 10.1039/b9nr00434c

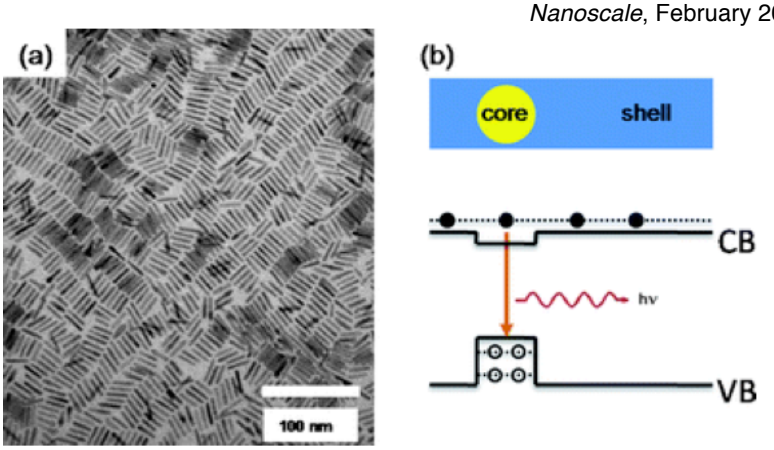

(a) A representative TEM image of CdSe/CdS core/shell quantum rods (QRs) with 5 nm diameter and 25 nm length. (b) A simplified sketch illustrating the band alignments and electronic levels within a CdSe/CdS core/shell QR.

ACS Nano, February 2010, 10.1021/nn9017334

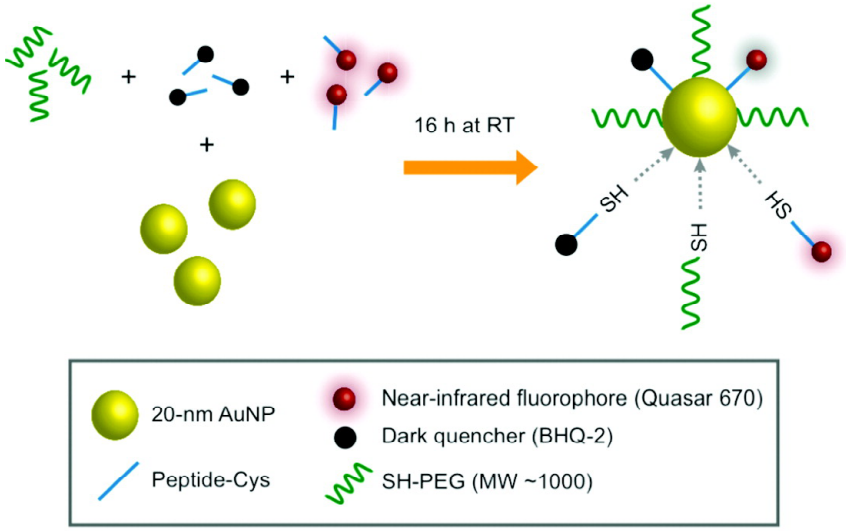

Figure 1 illustrates the one-step reaction method employed in synthesizing different mixed monolayer surfaces on the AuNP probes. Dye labeled peptides and SH-PEG were combined with AuNPs in a single 500 μL reaction mixture and rotated for 16 h at room temperature. The self-assembled AuNP probes were purified and separated from uncomplexed peptide substrate and SH-PEG by centrifugation and multiple washes with water.